Draft version August 7, 2015
Preprint typeset using LaTeX style emulateapj v. 5/2/11

EVOLUTION OF STAR-FORMATION PROPERTIES OF HIGH-REDSHIFT CLUSTER GALAXIES SINCE $Z = 2$

Seong-Kook Lee[1,5], Myungshin Im[1,5], Jae-Woo Kim[1], Jennifer Lotz[2], Conor McPartland[3], Michael Peth[4], Anton Koekemoer[2]

Draft version August 7, 2015

ABSTRACT

Using a stellar mass limited sample of $\sim 46,600$ galaxies ($M_* > 10^{9.1}\,M_\odot$) at $0.5 < z < 2$, we show that the stellar mass, rather than the environment, is the main parameter controlling quenching of star formation in galaxies with $M_* > 10^{10}\,M_\odot$ out to $z = 2$. On the other hand, the environmental quenching becomes efficient at $z < 1$ regardless of galaxy mass, and it serves as a main star formation quenching mechanism for lower mass galaxies. Our result is based on deep optical and near-infrared imaging data over 2800 arcmin^2, enabling us to negate cosmic variance and identify 46 galaxy cluster candidates with $M \sim 10^{14}\,M_\odot$. From $M_* \sim 10^{9.5}$ to $10^{10.5}\,M_\odot$, the fraction of quiescent galaxies increases by a factor of ~ 10 over the entire redshift range, but the difference between cluster and field environment is negligible. Rapid evolution in the quiescent fraction is seen from $z = 2$ to $z = 1.3$ for massive galaxies suggesting a build-up of massive quiescent galaxies at $z > 1.3$. For galaxies with $M_* < 10^{10}\,M_\odot$ at $z < 1.0$, the quiescent fraction is found to be as much as a factor of 2 larger in clusters than in field, showing the importance of environmental quenching in low mass galaxies at low redshift. Most high mass galaxies are already quenched at $z > 1$, therefore environmental quenching does not play a significant role for them, although the environmental quenching efficiency is nearly identical between high and low mass galaxies.

Subject headings: galaxies: clusters: general — galaxies: high redshift — galaxies: evolution — galaxies: stellar content — galaxies: star formation

1. INTRODUCTION

Galaxies define basic separate, independent entities in the universe and are the building blocks of her. Therefore, the study of their evolution throughout the history of the universe is the very core in our understanding of the universe.

The Λ cold dark matter (CDM) cosmological models say that galaxies form through the gravitational collapse of baryonic matters — mostly in the form of gas — inside dark matter (DM) halos. As gas collects within DM halos, it begins to cool and form stars, which gives galaxies the very glittering look as we observe them. An interesting question regarding star-forming (SF) activity of galaxies is how this activity evolves and what governs this activity. Unlike the collapse of DM, which is mainly governed by gravity, SF activity is governed or affected by various baryonic physical processes — including cooling of gas as well as feedbacks from stars, supernovae (SNe), or active galacitc nuclei (AGN) — thus making a detailed understanding of the SF activity complicated.

Regarding the evolution of SF activity of galaxies, we know that galaxies in the local universe have much lower levels of SF activity than the ones in the past. First, the global SF history, revealed from various galaxy surveys (Hopkins & Beacom 2006; Cucciati et al. 2012; Behroozi et al. 2013; Burgarella et al. 2013; Magnelli et al. 2013; Madau & Dickinson 2014) shows significant drop from redshift, $z \sim 1$ to $z \sim 0$ — with a possible broad peak around $z \sim 1 - 3$. While this shows the behavior of the collective SF activity in the universe, we can still speculate from this that the SF activity in individual galaxies must also decrease significantly. Second, star-formation rates (SFRs) of normal SF galaxies at $z \sim 0$ are significantly lower than SFRs of higher redshift ($z \gtrsim 1$) SF galaxies with similar mass (e.g., Daddi et al. 2007; Sobral et al. 2014). This suggests an average drop in SF activities of individual galaxies with time toward $z \sim 0$. Lastly, a large fraction of local galaxies — especially massive ones — are red, quiescent, and form a tight red sequence (e.g. Strateva et al. 2001; Blanton et al. 2003; Balogh et al. 2004). Therefore, we need to understand the physical mechanism(s) that can lower and eventually stop the SF activity of galaxies to explain this change of average SF properties of galaxies from high redshift to the local universe.

At low redshift, it has been well known that SFR, color and morphology of galaxies, show strong dependence on their mass (e.g. Kauffmann et al. 2003; Jimenez et al. 2005; Baldry et al. 2006), in such a way that less massive galaxies show more SF activities than massive ones. This clear mass-dependence seems to persist at higher redshift. By analysing the red-sequence luminosity function of a large sample (~ 500) of galaxy clusters at $z < 0.95$, Gilbank et al. (2008) found a dearth of red galaxies at faint luminosity at higher redshift. Recently, using the UltraVISTA (McCracken et al. 2012) data, Ilbert et al.

[1] Center for the Exploration of the Origin of the Universe, Department of Physics and Astronomy, Seoul National University, Seoul, Korea
[2] Space Telescope Science Institute, 3700 San Martin Drive, Baltimore, MD 21218, USA
[3] Institute for Astronomy, University of Hawaii, 2680 Woodlawn Drive, Honolulu, HI 96822, USA
[4] Department of Physics and Astronomy, Johns Hopkins University, 3400 North Charles Street, Baltimore, MD 21218-2686, USA
[5] sklee@astro.snu.ac.kr, mim@astro.snu.ac.kr

(2013) have shown the stellar-mass dependence in SF quenching at $z < 1$ in a sense that stellar mass density of massive ($> 10^{11.2} M_{\odot}$) quiescent galaxies remains unchanged while less massive galaxies keep being quenched — i.e., massive ones already quenched before $z \sim 1$, earlier than less massive ones. The origin of this mass-dependent SF cessation or quenching is still unclear. It could be the effect of feedback from AGN (Hopkins et al. 2006; Somerville et al. 2008), which is believed to selectively act for more massive galaxies. Another compelling explanation is the heating of accreted cold gas in massive halos (Birnboim & Dekel 2003).

On the other hand, the SF activity — or related properties, such as color or morphology — shows environmental dependence as well. Locally, galaxies show distinct SF properties and colors in different environment (Lewis et al. 2002; Kauffmann et al. 2004; Blanton et al. 2005). Naturally arising questions are how and when these environmental trends have been developed. By analysing galaxy colors out to $z \sim 1.5$ from VIMOS-VLT Deep Survey (VVDS), Cucciati et al. (2006) found that the color–density relation progressively weakens with increasing redshift and possibly reverses at $1.2 < z < 1.5$. Grützbauch et al. (2011), based on the Palomar Observatory Wide-Field Infrared (POWIR; Conselice et al. 2008) survey data in the DEEP2 field, also argued that there is no or weak correlation between galaxies' local number density and the color or the blue galaxy fraction for $0.4 < z < 1$ galaxies. In the case of the relation between SFR and density, Cooper et al. (2008) found the reversal of the relation between SFR and overdensity at $z \sim 1$ using galaxy samples from the DEEP2 Galaxy Redshift Survey (GRS). With GOODS data, Elbaz et al. (2007) also argued that the relation between SFR and density was reversed at $z \sim 1$, showing a sharp contrast to the local trend.

On the contrary, Cooper et al. (2006) argued that the mean galaxy environment shows a strong dependence on galaxy color at $z \sim 1$, similarly with what is locally found. Patel et al. (2009), analysing $z \sim 0.8$ galaxies, found that the total SFR–local-density relation still persists at this redshift. This environmental dependence of galaxy properties has been shown to persist even at higher redshift ($z < 2$) by Quadri et al. (2012), through the analysis of quiescent galaxy fraction of UKIDSS/UDS galaxies, even though the environmental trend of quiescent fraction becomes weaker with redshift. Combining data from several surveys — UltraVISTA, 3D-HST (Brammer et al. 2012), Cosmic Assembly Near-infrared Deep Extragalactic Legacy Survey (CANDELS; Grogin et al. 2011; Koekemoer et al. 2011), and SDSS, Tal et al. (2014) have studied the evolution of quiescent galaxy fraction in groups over a wide range of redshift up to $z < 2.5$. Their finding is that quiescent fraction of group satellite galaxies is similar with background (i.e. field) galaxies at $z \sim 2$, while it increases faster than field galaxies at lower redshift down to $z \sim 0$. So, there seems to exist a certain degree of disagreement on how and how much the environmental trend changes as we go up to high redshift, even though there is a consensus on the fact that the environmental dependence weakens as redshift increases (e.g., Scoville et al. 2013). Therefore, we have not yet reached to a firm conclusion about the rate or amount of evolution in the effects of environment on the formation and evolution of the quiescent galaxy population.

In studying the role of environment in formation and evolution of quiescent galaxies, galaxy cluster offers a very unique laboratory. They define the densest galaxy environment, thus are expected to follow the highest density peaks in the universe. Besides the fact that denser structures collapse earlier in the ΛCDM paradigm, galaxies in these dense environments would also be subject to several physical processes — such as ram-pressure stripping (Gunn & Gott 1972), strangulation (Larson et al. 1980; Balogh et al. 2000), and harassment (Moore et al. 1998) — acting exclusively in group- or cluster-like environments. In this regard, studying the stellar population properties of galaxies in galaxy clusters at various redshifts is a useful and crucial test bed in the investigation of the environmental effects on the formation and evolution of quiescent galaxy population.

While there is a sharp contrast in galaxy properties between galaxies in clusters and in field locally, as the cluster environment is dominated by the red, quiescent galaxies (e.g., Dressler 1980), this picture seems to change as we go out to high redshift (Butcher & Oemler 1984; Dressler et al. 1997; Poggianti et al. 2001). Combining their field sample with the cluster samples from Holden et al. (2007), van der Wel et al. (2007) showed that the difference in the red galaxy fraction between the cluster- and the field environments increases with decreasing redshift — i.e., the red galaxy fraction increases toward low redshift in the cluster environment while it remains nearly constant in the field environment. At higher redshift, $z > 1.5$, the story seems to become more complicated: Studies suggest that the galaxy SF properties (the SFR or the color) in the cluster environment at $z > 1.5$ can be different from those of cluster galaxies at lower redshift and that there can be cluster-to-cluster variation in the properties of these high-redshift proto-clusters. Gobat et al. (2011) analysed colors of red galaxies in a proto-cluster at $z \sim 2.1$ originally identified by their red *Spitzer*/IRAC colors, and find that these red galaxies have old stellar populations. On the other hand, Zirm et al. (2008) found a well developed red-sequence in a $z \sim 2.2$ proto-cluster around a radio galaxy and suggested that many of these red galaxies are porbably dusty star-forming galaxies. Fassbender et al. (2011) also reported the existence of the actively star-forming galaxies in the X-ray selected proto-cluster at $z \sim 1.6$. Tran et al. (2010) studied the color and SF properties of the member galaxies of *Spitzer*-selected $z \sim 1.6$ cluster (Papovich et al. 2010). They also found that the galaxies in this high redshift cluster, unlike the ones in lower redshift, are more dominated by blue galaxies. This, combined with the higher star-forming galaxy fraction within this cluster than in the lower redshift ($z \sim 0.3$), indicates that many cluster galaxies are still actively forming stars at $z \sim 1.6$. The results of Hilton et al. (2010), based on the X-ray and mid-IR (MIR) observation, also show the strong SF activity of the cluster member galaxies at $z \sim 1.5$. Strazzullo et al. (2013) have found that there are massive star-forming galaxies along with passive ones even in the core region of the IRAC-selected $z \sim 2.1$ proto-cluster studied by (Gobat et al. 2011). All together, these observational results point to the redshift range of $z > 1.5$ as the active formation era of the galaxy

clusters as well as the epoch when many of cluster galaxies are still forming stars actively.

Summarizing, both the mass and environment of galaxies seem to affect the quenching of SF activity of galaxies and the formation of quiescent galaxies. Also, the environmental dependence of SF activity of galaxies seems change with redshift. Therefore, more investigation about the timing (i.e., the redshift dependence) as well as the relative contribution from these distinct mechanisms — mass versus environment — is still needed. Peng et al. (2010) have provided interesting results in this regard. Using SDSS (York et al. 2000) and zCOSMOS (Lilly et al. 2007) data, they analysed the effects of mass as well as environment on the evolution and star-formation activity of galaxies at redshifts up to $z \sim 1$. They found that "mass quenching" is more dominant for high stellar-mass ($\gtrsim 10^{10}\ M_{\odot}$) galaxies, while lower mass galaxies are more affected by "environmental quenching". They also suggested that the combination of these two quenching mechanism can explain the evolution of stellar mass function of star-forming as well as quiescent galaxies. Analysing $z \sim 1$ Hα emitters from the High-z Emission Line Survey (HiZELS), Sobral et al. (2011) have shown that the median SFR depends on galaxies' environment for galaxies with their stellar mass lower than $10^{10.6}\ M_{\odot}$, while there is no environmental dependence for more massive galaxies.

In this work, we extend this kind of investigation to higher redshift (up to $z \sim 2$), examining the effects of these two suggested drivers — i.e. mass and environment — in the formation and the evolution of quiescent galaxy population. It has been known that a tight red sequence already exists at $z \sim 1$ (e.g. Im et al. 2002; Bell et al. 2004). Therefore, investigation at higher ($z > 1$) redshift is crucial in catching the formation of these quiescent galaxies to place a meaningful constraints on their evolution. Our work is based on the deep near-infrared (NIR) data from the United Kingdom Infrared Telescope (UKIRT) Infrared Deep Sky Survey (UKIDSS) Ultra Deep Survey (UDS) as well as deep optical data from the Subaru/XMM-Newton Deep Survey (SXDS), combined with mid-IR (MIR) data from the *Spitzer* Space Telescope. Deep UDS NIR data are crucial in robust estimation of SF or stellar population properties of galaxies, breaking the degeneracy between old and dusty star-forming populations, thus in a study of quiescent galaxy population evolution at redshift as high as $z \sim 2$. Our analysis is based on (1) an un-biased cluster detection (unlike, for example, the red-sequence method), (2) a relatively long redshift-baseline ($0.5 \lesssim z \lesssim 2.0$) and a large spatial area (~ 665 Mpc^2 at $z \sim 1$), and (3) robust estimation of SFR and stellar mass from SED-fitting. As demonstrated below, deep NIR data in the UDS field enables us the robust estimation of the stellar population properties of the galaxies up to $z \sim 2$.

We present the data set used in this work as well as the sample selection procedure in Section 2. In Section 3, we explain how the photometric redshifts as well as the stellar population properties of the UDS galaxies are estimated. We explain the identifying procedure of the high-redshift clusters and provide the properties of the selected cluster candidates in Section 4. We analyse the stellar population properties and the evolutionary trends of the quiescent galaxies, focusing on the drivers of this population in Section 5, and we summarize our results in Section 6. We adopt the standard flat ΛCDM cosmology, with $(\Omega_m, \Omega_\Lambda) = (0.3, 0.7)$, and $H_0 = 70\ km\ s^{-1}\ Mpc^{-1}$. All magnitudes are given in AB magnitude system (Oke 1974) except when otherwise mentioned.

2. DATA AND SAMPLE

The UDS (Almaini et al. in prep.), which is one of the five surveys in the UKIDSS (Lawrence et al. 2007), provides a very deep NIR imaging dataset over an area of ~ 0.77 degree^2 located on the SXDS. The survey was carried out with the Wide Field Camera (WFCAM; Casali et al. 2007) on the UKIRT in three NIR broad-bands with the 5-σ limits of $J = 24.3$, $H = 23.3$, and $Ks = 23.0$ (in Vega, DR10).

The SXDS provides the deep optical data from the SUPRIMECAM on the Subaru telescope from B-band through z'-band. The 3-σ depths of the Subaru data are $B = 28.4$, $V = 27.8$, $R = 27.7$, $i' = 27.7$, and $z' = 26.7$. We use the released DR1 (z'-band detected) catalog (Furusawa et al. 2008), which is obtained from the SXDS DR1 release page[6], for this work. The UDS region has also been observed by the *Spitzer*/IRAC as the SpUDS Spitzer Legacy Survey (PI:Dunlop), reaching ~ 24 magnitude (Channels 1 and 2). We obtain the catalog at the Spitzer Legacy Survey archive[7], and aperture-corrected total magnitudes are used for *Spitzer*/IRAC data. We also use the publicly available spectroscopic redshift data for about 4000 objects (Simpson et al. in prep, Akiyama et al. in prep. and Smail et al. 2008)

We perform photometry on the UDS DR10 images (J, H, Ks) using SExtractor (Bertin & Arnouts 1996) software. We use 9×9 convolution mask of a Gaussian PSF with FWHM of 5 pixels, and set the detection minimum area as 6 pixels. The detection and photometry are done in each band separately, and then the match between different bands is done with a matching radius of $1''$ and with the Ks-band image as the reference image. About 0.8% objects (both in J- and H-band catalogs) have multiple matches, and the nearest one is selected as the best match. To construct the panchromatic spectral energy distributions (SEDs) from the optical to the MIR in the observed frame, we match, first, the Subaru optical and UDS NIR catalogs, and then with the SpUDS IRAC catalog, with a matching radius of $1''$ and the position in Ks-band catalog is used as the reference position. For optical and NIR data, we use the auto magnitudes, and the aperture-corrected total magnitudes are used for IRAC data.

We check the validity of using auto magnitude ($Mag_{\rm auto}$) in crowded region, such as clusters, by comparing auto magnitude values with aperture (circular diameter = $1\farcs5$) magnitude ($Mag_{\rm aper}$) in field and cluster regions. If $Mag_{\rm auto}$ values are biased in cluster regions, then we expect that $Mag_{\rm auto}$ to deviate from $Mag_{\rm aper}$ differently in cluster and field. At several magnitude bins ($Ks = 19.9, 20.9, 21.9, 22.9$), we compare the distributions of $Mag_{\rm aper} - Mag_{\rm auto}$ between cluster and field region through the Kolmogorov-Smirnov test (K-S test). At each magnitude bin, the maximum difference, D, was

[6] http://soaps.nao.ac.jp/SXDS/Public/DR1/
[7] http://irsa.ipac.caltech.edu/data/SPITZER/SpUDS/

0.073, 0.086, 0.071, 0.058, and the probability of null hypothesis, p, was 0.93, 0.62, 0.64, 0.94, showing that there is no systematic bias in auto-magnitude measurements that is specific in cluster region.

In our analysis, we use objects which are detected in both of optical (Subaru) and NIR (UKIRT) catalogs as our sample, but regardless of IRAC detection. There are about 8.4% of Ks-band detected objects not detected in z' band. The fraction is lower as 5.9% if we only consider the sources with $Ks \leq 24.9$. These z'-band undetected sources have, on average, redder IR colors than the detected ones. The mean values of $(J - Ks)$ and $(J - 3.6\mu m)$ are 1.0 and 1.8, respectively, while the corresponding values are 0.6 and 1.0 for z'-band detected objects. And, about 25% of Ks- and z'-bands detected objects are matched with IRAC sources.

From this 'Subaru+UKIRT+Spitzer' multi-band photometric catalog, we first cull out stars either based on the spectroscopic classification or broad-band color (BzK or J-K). Specifically, from $\sim 200,000$ total objects, we exclude: (1) ~ 550 spectroscopically classified stars, (2) $\sim 22,000$ stellar candidates based on their location in the (B-z')–(z'-Ks) color–color plane, with the color criterion of $(z' - Ks) < 0.3 \times (B - z') - 0.4$, similarly with Daddi et al. (2004) or Hanami et al. (2012), and (3) further ~ 500 candidates with $J - Ks < 0$ and $Ks < 19.0$, based on the fact that galaxies and stars form clearly separate branches in this $J - Ks$ versus Ks plane.

We need to cull out active galactic nuclei (AGN) from our sample because the measurements of photometric redshift and stellar population properties, which are crucial in our study, would be affected by the AGN activity. To remove AGN candidates from this star-removed, multi-band catalog, we use three steps: First, we exclude 77 objects which are classified as quasars in the spectroscopic catalogs. Next, we match our multiband catalog with the XMM-Newton point source catalog (Ueda et al. 2008) to remove any matched object. At this step, about 220 objects are matched and excluded. Finally, for the objects with the matched IRAC photometry, we use the NIR & MIR color criteria suggested by Messias et al. (2012) to find out any remaining AGN candidates. The applied criteria are $(K - m_{4.5}) > 0$ and $(m_{4.5} - m_{8.0}) > 0$, where, $m_{4.5}$ and $m_{8.0}$ are the magnitudes in IRAC channel 2 ($4.5\mu m$) and channel 4 ($8.0\mu m$), respectively. About 7,000 objects satisfy these color criteria, thus are excluded from the sample. These color criteria, similarly with other IRAC color criteria, cannot distinguish between AGN and high-redshift ($z > 2$) galaxies. Therefore, by applying these criteria, we might lose some non-active galaxies at $z > 2$ as well. However, this does not affect our results, because our target redshift range does not exceed $z \sim 2$.

After trimming out AGN candidates as well as stars as explained, we apply the Ks-band magnitude cut ($Ks \leq 24.9$, 5 σ detection limit) and the number of remaining galaxies is about 115,000 among which ∼1,400 objects have spectroscopic redshift information. For these ∼115,000 objects, we derive photometric redshifts as well as stellar population properties through SED-fitting (Section 3). After selecting galaxies within the redshift range of $0.45 \leq z \leq 2.1$ and applying the stellar mass cut of $\log M_*/M_\odot \geq 9.1$ — which is the 75% stellar mass limit at the highest redshift bin ($z \sim 2$) of our study — our final sample size is 46,641.

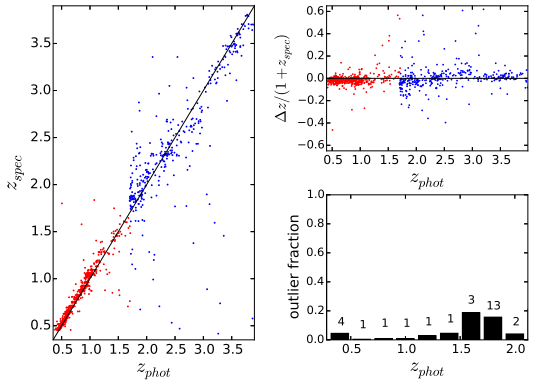

Figure 1. **(left)** Comparison of spectroscopic and photometric redshifts for the subset of UDS (red) and GOODS-S (blue) galaxies with available spectroscopic redshift. **(upper right)** Photometric redshift discrepancy as a function of redshift. **(lower right)** Outlier ($|\Delta z|/(1 + z_{spec}) > 0.15$) fraction as a function of redshift. Numbers above each bar show the number of outliers at each redshift bin.

3. ESTIMATION OF PHOTOMETRIC REDSHIFTS AND STELLAR POPULATION PROPERTIES

3.1. *Photometric Redshift*

We derive photometric redshifts using the EAZY code (Brammer et al. 2008). We take the K-band magnitude prior, which slightly improves the photometric redshift accuracy. We fit ten broad-band photometric data points from the observed frame optical (Subaru) to MIR (*Spitzer*/IRAC). During the fitting procedure, we require that at least five colors to be measured — i.e. it is detected at least at six bands. Therefore, any galaxy which is not detected at more than five bands is not included in the following analysis. Only $\sim 0.14\%$ of objects are excluded for this reason, and these are mostly faint objects — $K > 24$ for $\sim 72\%$ among these, and $z' > 26$ for $\sim 52\%$.

For a subset of galaxies for which spectroscopic redshifts are available and $Ks < 24.9$, we compare the spectroscopic and the photometric redshifts to estimate the accuracy of the photometric redshift (Figure 1, left panel). In UDS, there are not enough galaxies with $z_{spec} > 1.5$ for a fair estimation of photometric accuracy. To test the photometric redshift accuracy at $z \gtrsim 1.5$, we use the GOODS-S data, which carries similar coverage of broad-bands data with the UDS while having more abundant spectroscopic redshift samples at $z \gtrsim 1.5$. These GOODS-S spectroscopic data are from various spectroscopic surveys (Le Fèvre et al. 2004; Szokoly et al. 2004; Mignoli et al. 2005; Cimatti et al. 2008; Vanzella et al. 2008; Popesso et al. 2009; Balestra et al. 2010; Silverman et al. 2010). We measure signal-to-noise of UDS photometric data as a function of magnitude at each band, and add additional noises (randomly following a Gaussian distribution) to the GOODS photometry to simulate the depth of the UDS data. Then, photometric redshifts are derived using these noise-added photometry. Within the redshift range of $0.4 \leq z \leq 2.1$, the redshift range of interest of this work, there are 3% of objects whose redshift

error, defined as $|\Delta z|/(1+z_{spec})$, is greater than 0.15. Removing these objects with catastrophic redshift errors, the mean error is 0.028.

The right panels of Figure 1 show $|\Delta z|/(1+z_{spec})$ as well as the outlier fraction as functions of photometric redshift. We can see that our photometric redshift estimation is reliable within the redshift range of our study, $0.5 \lesssim z \lesssim 2$, but its uncertainty is larger at $z > 1.5$. The outlier fraction increases at high redshift ($z > 1.5$), but it is kept at < 0.2. The reason for the increase in the photometric redshift uncertainty at $z > 1.5$ is that the spectral break at ~ 4000 Å — one of the clearest redshift indicators — moves out of the optical regime at $z > 1.5$. When that happens, it becomes more difficult to sample the exact location of the rest-frame 4000 Å break in the observed frame due to the gaps between NIR filters and the reduced number of available filters above 4000 Å break. Also, the fraction of star forming galaxies are higher at $z > 1.5$ in the spectroscopic sample since it is easier to spot emission lines than absorption lines for faint galaxy spectra. Weak 4000 Å breaks and strong emission lines of star forming galaxies make it difficult to trace the continuum shape, leading to a reduced accuracy in photometric redshifts (e.g., Damen et al. 2009; Ilbert et al. 2009; Quadri et al. 2012; Hartley et al. 2014; Yang et al. 2014; Kang & Im 2015). Not surprisingly, photometric redshift outliers tend to be star-forming galaxies, and some of them can move into the red sequence due to the large errors in photometric redshift.

In Figure 2, we show the z_{spec} distribution of galaxies with several z_{phot} bins ($z \sim 0.6, 0.8, 1.0, 1.2, 1.4$ and 1.6) with $|\Delta z| \leq 0.1$. Figure 2 shows that systematic offsets between photometric and spectroscopic redshifts are small ($\lesssim 0.1$ at some redshift bins). The effect of the small systematic shift in redshift is negligible in our analysis. For example, a systematic offset of $\Delta z \sim 0.1$ causes a shift in the stellar mass estimate by $< 20\%$.

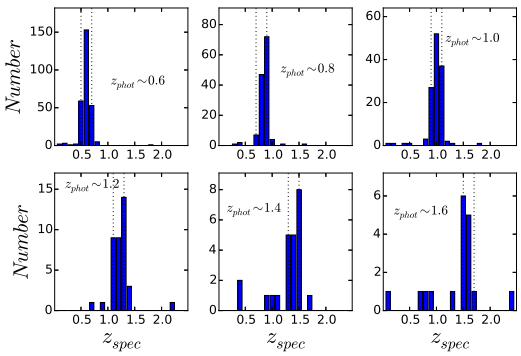

Figure 2. Distributions of spectroscopic redshift of galaxies selected by their photometric redshift at various redshift bins. For example, at redshift 0.6, this figure (upper left panel) shows the distribution of spectroscopic redshifts of galaxies whose photometric redshifts are within $0.5 \leq z_{phot} \leq 0.7$. Systematic offsets are small, if there is any (¡ 0.1), between photometric and spectroscopic redshifts. The fraction of redshift outlier increases at higher redshift while the number of ourliers remain similar.

3.2. *Stellar Population Properties from SED-fitting*

We perform the stellar population analysis through spectral energy distribution (SED) fitting methods for our sample, with the same procedure as explained in detail in Lee et al. (2009, 2010). For redshift, we adopt z_{spec} if available, but z_{phot} otherwise.

The stellar population synthesis models of Bruzual & Charlot (2003, BC03, hereafter) with Padova 1994 stellar evolutionary tracks are used for our SED-fitting analysis. We assume the Chabrier (2003) initial mass function (IMF) with the lower and upper mass cuts of 0.1 and 100 $M_{\odot}$.

As for the star-formation histories (SFHs), we use the delayed SFHs (Lee et al. 2010). This form of SFH is shown to provide better estimation of stellar population properties than other forms, for example, exponentially declining ones (e.g. Maraston et al. 2010; Papovich et al. 2011; Pforr et al. 2012; Lee et al. 2014). Studying $z \sim 1$ galaxies from DEEP2 Redshift Survey (Newman et al. 2013), Pacifici et al. (2013) have also shown that these galaxies have SFHs similar with this form.

It has the following functional form.

$$\Psi(t,\tau) \propto \frac{t}{\tau^2} e^{-t/\tau}, \quad (1)$$

where, $\Psi(t,\tau)$ is the instantaneous SFR for a given set of τ and t. The parameter t is the time since the onset of the star-formation and τ is the time-scale parameter which governs how fast (or slowly) the SFR reaches its peak value before starting to decline. We allow the value of τ to vary within a very broad range from 0.1 Gyr to 10.0 Gyr, and t within 0.1 Gyr $\leq z \leq t_H(z)$, where $t_H(z)$ is the age of the Universe at redshift z.

After extracting $\sim$ 4,000 spectral templates from BC03 with these allowed values of parameters, we apply the Calzetti et al. (2000) attenuation law to model the dust attenuation of SEDs due to the inter-stellar dust. We vary the amount of attenuation, parametrized via $E(B-V)$ within $0.0 \leq E(B-V) \leq 1.50$ with the increment of 0.025. For the attenuation due to the line-of-sight neutral hydrogen in the inter-galactic medium (IGM), we apply the extinction law of Madau (1995). During the fitting, the redshift is fixed at the value of the spectroscopic redshift if available, otherwise at the photometric redshift.

We apply the 'grid-scanning' method which has been used in several previous works (Wiklind et al. 2008; Lee et al. 2009, 2010, 2014). As explained in these references, our method of skimming the entire parameter space is less subject to the effects of any prior. From this SED-fitting results, we derive for each galaxy, the stellar mass (M_*), the SFR, the mean age of the stellar population, the amount of dust attenuation ($E(B-V)$), as well as the star-formation history — parametrized in terms of τ and t. The SFR used in this work is defined as the SFR averaged over recent 100 Myr, based on the reasoning outlined in Lee et al. (2009). We also derive the rest-frame $u-g$ color — will be denoted as $(u-g)_0$ from now on — for each galaxy from its best-fit BC03 template.

The broad wavelength coverage out to IR regime as well as the deep optical data from Subaru in the UDS field enables us to estimate the stellar population properties of high-redshift galaxies with high confidence and distinguish dusty SF galaxies from old galaxies among red galaxies. Figure 3 shows the examples of the SED-

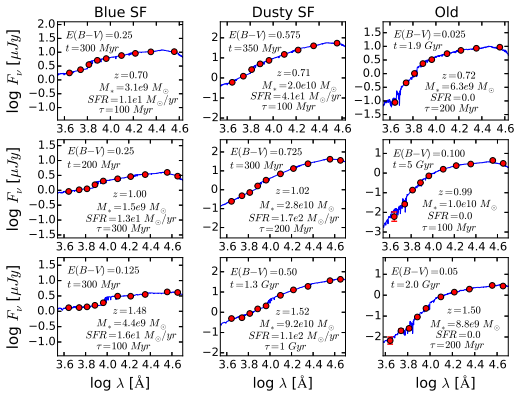

Figure 3. Examples of observed SEDs and the best-fit BC03 spectrum for blue SF (**left column**), dusty SF (**middle column**), and old passive (**right column**) galaxies at $z \sim 0.7$, 1, 1.5. In each panel, red circles show the observed fluxes from $BVRiz$ (Subaru) to $JHKs$ (UKIRT) to MIR (Spitzer) upto IRAC Channel 2 (4.5 μm). Solid blue curve is the best-fit BC03 spectrum found through SED-fitting. We can see that blue SF galaxies have bluer colors than red, dusty SF galaxies throughout the shown wavelength range as well as that dusty SF galaxies and old quiescent ones can be discriminated reliably thanks to the deep and wide wavelength coverage of the data. Wavelength (x-axis) is in logarithmic scale of Å, and flux is in log-scale of μJy.

fitting results for a representative set of galaxies at various redshifts. Also shown are the key SED-fit parameters. In this figure, we show the observed galaxy SEDs (red circles) as well as the best-fit BC03 spectra for typical blue SF galaxies (panels in left column), dusty SF ones (panels in middle column) and old quiescent ones (panels in right column) at redshifts $z \sim 0.7$, 1, 1.5.

Here, we define "quiescent galaxies" as galaxies with sSFR $< 1/[3t(z)]$ yr^{-1}, where $t(z)$ is the age of the universe at z. This cut was used in several previous works (e.g., Damen et al. 2009), and approaches the local value for sSFR cut at $z \sim 0$ (e.g., Gallazzi et al. 2009; Ko et al. 2014). Under a delayed SFH model (i.e., Equation (1)), $1/[3t(z)]$ corresponds to $\sim 1\%$ of the peak SFR. While this sSFR cut select galaxies with low SF activity in comparison to the average SF galaxies at that redshift, the selected galaxies can have SFRs that are not quite "quiescent". For example, at $z \sim 2$, $M_* \sim 10^{11} M_\odot$ galaxies at the sSFR cut have $\sim 10 M_\odot$/yr — i.e., SFR of starburst galaxies in the local universe. If we fit the SEDs of a 1 Gyr-old, passively evolving galaxies after a spontaneous burst (a truly quiescent galaxy at high redshift), our procedure returns sSFR $\sim 10^{-11}$ yr^{-1}. We check the MIPS 24 μm detection of our galaxies using SpUDS MIPS catalog. We find that small fraction ($\sim 5\%$) of red SF galaxies is detected, while no quiescent galaxy is detected at 24 μm.

We test how the error in photometric redshift measurement may affect the estimation of stellar masses of galaxies using Monte Carlo simulation. Specifically, first, we scatter the redshift of each galaxy assuming a Gaussian distribution of redshift error. Then we repeat SED-fitting by fixing the redshift at this scattered value. We repeat this procedure 100 times each galaxy at $z \sim 1$ and $z \sim 1.5$, within a redshift range ± 0.02. The results of this simulation are given in Figure 4, where we show the number counts of galaxies at stellar mass bins. The resulting number distributions with scattered redshift (red) show no significant difference from the ones without scatter (blue) at both redshift bins. For individual galaxies, the mean and the standard deviation of $\Delta M_*/M_{*,true}$ is 0.02 ± 0.11 and 0.01 ± 0.09, at $z \sim 1$ and ~ 1.5, respectively. Here, ΔM_* is $M_{*,MC} - M_{*,true}$, and $M_{*,true}$ is the measured stellar mass without redshift scatter. From this, we can ensure that the stellar mass is not significantly affected by the error in photometric redshift measurement.

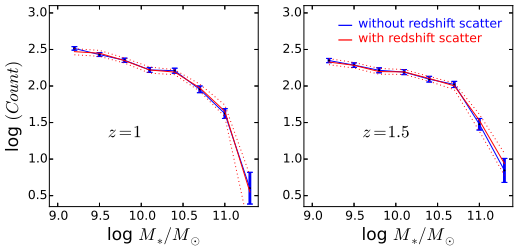

Figure 4. Galaxy number counts (and error) at stellar mass bins (blue) and the same ones but with photometric redshift scatter effect included (red) at $z = 1$ (left) and $z = 1.5$ (right). Red solid and dotted lines in each panel show the mean and envelope (i.e. minimum and maximum) of Monte Carlo simulation (100 times) which include the redshift scatter. We can see that the effect of photometric redshift error is not significant in the estimation of the stellar mass function.

4. MASSIVE STRUCTURES OF GALAXIES

4.1. *Stellar Mass Limit*

Based on the stellar mass derived from the SED-fitting, we select galaxies with their stellar masses greater than $10^{9.1}$ $M_\odot$ (which is the 75% stellar mass limit at the highest redshift range, $z \sim 2.0$) within the redshift range of $0.45 \leq z \leq 2.1$.

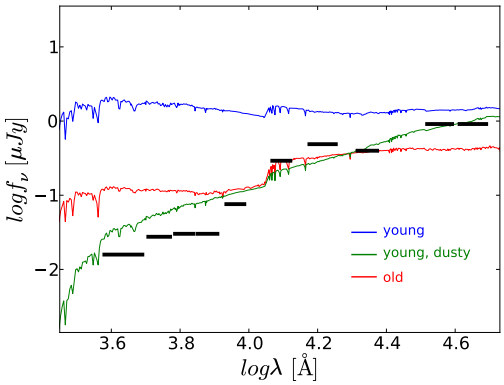

Figure 5. Depths of the datasets used for our study, in comparison to different types of galaxies. Black horizontal bars show the flux limit of the UDS in 5 Subaru filters (B, V, R, i', z'), 3 UKIRT filters (J, H, Ks), and 2 IRAC channels (3.6μm, 4.6μm). All the galaxy templates are normalized to have stellar mass of $10^{9.1} M_\odot$. Solid blue curve shows the spectrum of a young galaxy template with $t = 200$ Myr with no dust attenuation. Solid green curve is for the same galaxy template but with high dust attenuation value of $E(B-V) = 0.4$. Red curve shows an old, quiescent galaxy template with $t = 2$ Gyr — maximally possible age at $z = 2$ if we assume the formation redshift as $z_{form} = 5$. This figure shows that we can detect with our data set galaxies at $z \sim 2$ with stellar mass as low as $\sim 10^{9.1}$ $M_\odot$.

We have checked if the magnitude limit is deep enough to detect galaxies with stellar mass of $10^{9.1} M_\odot$ out to

$z = 2.0$, using galaxy template spectra of various galaxy types extracted from the BC03 library. In Figure 5, we show these spectra — young (solid blue curve), dusty young (solid green curve), and old (solid red curve) — with stellar mass of $10^{9.1} M_\odot$ and redshifted to $z = 2.0$. We also show the limiting flux of the UDS data set in 5 Subaru optical filters (B, V, R, i', and z'), in 3 UKIRT filters (J, H, and Ks) and in 2 IRAC channels ($3.6\mu m$ and $4.5\mu m$) shown as black horizontal bars. We find that SEDs of all the galaxy types are above the detection limits in multiple bands, demonstrating that our dataset is nearly suitable for selecting galaxies with log $(M_*/M_\odot)$ > 9.1.

Figure 6 shows the redshift versus stellar mass of galaxies in the K-band limited sample. In this figure, the green vertical lines show the sample redshift range of this study and the green horizontal lines show the stellar mass limits. Blue curve shows the stellar masses at different redshifts of star-forming galaxy templates from BC03 with formation redshift of $z_f = 3$. Yellow curve corresponds to quiescent galaxy templates with $z_f = 5$, which is a reasonable formation redshift for faint/low-mass galaxies, while red curve is for galaxy templates with extremely high formation redshift ($z_f = 10$). As shown in this figure, within the given redshift range, we can detect log $(M_*/M_\odot) \gtrsim 9.1$ galaxies (corresponding lower green horizontal line) either quiescent (yellow curve) or star-forming (blue curve). It is still possible that we may miss some low mass ($< 10^{9.5} M_\odot$) galaxies with extremely old ($z_f \sim 10$) population, even though it is reasonable to assume that there are only few, if any, galaxies with these extreme properties in reality. For this reason, we apply the stellar mass cut of $10^{9.5} M_\odot$ (upper green horizontal line) when we deal with quantities which might be affected by this missing of low-mass old galaxies. Within this redshift range and above the stellar mass limit (log $(M_*/M_\odot) = 9.1$), we have 46,641 galaxies.

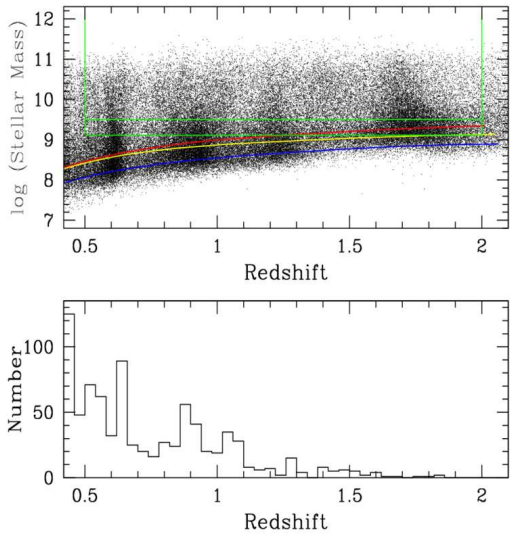

Figure 6. (Top) Redshift versus stellar masses derived from the SED-fitting. Green lines show the redshift range (vertical) as well as the stellar mass limits (upper horizontal: near 100% at $z < 2$; lower horizontal: near 100% at $z < 1.5$ and 75% at $z < 2$) of our sample. Solid curves shows the stellar mass at different redshift of quiescent (yellow and red) and SF (blue; $z_f = 3$) BC03 galaxy templates with $K = 24.9$. The yellow and red curves correspond to quiescent galaxies with reasonable ($z_f = 5$) and extreme ($z_f = 10$) formation epoch, respectively. This figure illustrates that we can detect reasonably old galaxies with log $(M_*/M_\odot) = 9.5$ up to $z = 2$, while we may miss some extremely old, low-mass galaxies, if any. **(Bottom)** Distribution of spectroscopic redshift. It shows peak near $z \sim 0.6$ and ~ 0.9 similarly as total (photometric redshift) sample as shown in top panel. The number of spectroscopic sample quickly drops at $z > 1$.

4.2. *Method and Procedure*

Our method of finding galaxy cluster candidates is based on the photometric redshift and similar with the method used in Kang & Im (2009, 2015). Following is the detailed explanation of the procedure we use to identify the cluster candidates. First, we divide the projected sky area into retangular grids with a width of $12''$, which corresponds to ~ 96, 102, and 100 kpc at $z = 1$, 1.5, and 2. Then, at a given redshift bin and at each grid point, we count the galaxies with log $(M_*/M_\odot) \geq 9.1$ within a radius of $r \leq 700$ kpc ($\sim 1.5'$ at $z \sim 1$) from the grid point within the redshift range of the typical redshift error in the UDS (i.e., $\Delta z = \pm 0.028 \times (1 + z)$). We repeat this procedure at redshift bins with an increment of Δz $= 0.02$.

Next, we find the mean ($\bar{N}$) and the standard deviation (σ_N) of the galaxy number counts (N) through the Gaussian fitting at each redshift bin. Then, we identify the *over-dense* grid points with their galaxy number counts that exceed the 4-σ level from the mean, i.e.,

$$N \ \geq \ \bar{N} + 4 \times \sigma_N. \qquad (2)$$

If we see the spatial distribution of these *over-dense* grid points with extreme galaxy number counts ($\geq 4\sigma$), we find that some points are connected to other points making large structure while some points are relatively isolated. In our case, the spacing between the grid points ($\sim$ 100 kpc) is much smaller than the typical size of galaxy clusters ($\sim$ 1 Mpc). Therefore, a cluster of galaxies would appear as a structure with connected *over-dense* grid points. For example, if 9 grid points are connected with each other with a square shape (i.e., 3×3) or if 10 grid points are connected in a rectangular shape (i.e., 2×5), this connected structure would represent an overdense structure with a radius of $\sim 850 - 900$ kpc. Based on this reason, we exclude any *over-dense* grid points when the number of connected grid points is smaller than 10 at each redshift bin. Then, among the remaining connected structures, we only select the structures as our final (proto-)cluster candidates only when these structures are identified at the same sky location (within the displacement, $d \leq 1.5$ Mpc) in at least three successive redshift bins. In other words, if the connected structure is found only in one or two redshift bin(s), we discard this structure. This criterion has been applied to minimize any false detection of cluster candidate. By applying these two, rather conservative criteria in selecting cluster candidates, we try to make our selection of cluster sample as robust as possible. By comparing with a mock catalog from the GALFORM simulation (Merson et al. 2013), we find that our cluster finding method is nearly complete at selecting $M_h > 10^{13.8} M_\odot$ clusters at $z \sim 0.9$ and $z \sim 1.5$. A detailed description of this method applied on simulation data can be found in Kang & Im (2015).

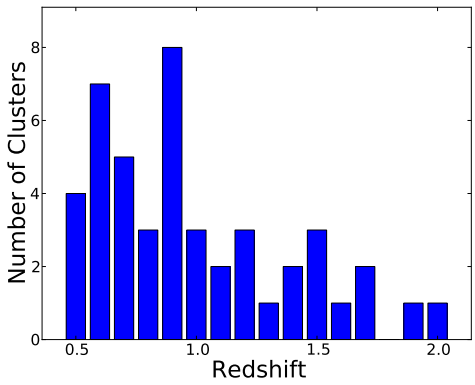

Figure 7. The number of identified cluster candidates within the redshift range of $0.5 \lesssim z \lesssim 2.0$.

4.3. *Galaxy Cluster Candidates*

Following the procedure as explained in the previous section, we find 46 cluster candidates within the redshift range of $0.5 \lesssim z \lesssim 2.0$. Among these, 19 clusters are the ones already identified by other authors (van Breukelen et al. 2006, 2007; Finoguenov et al. 2010; Papovich et al. 2010) in the same UDS-field, and 27 clusters are newly identified in this work. Figure 7 shows the number of the cluster candidates at each redshift bin.

In Table 1, we present the basic properties of these cluster candidates, including the number of member galaxies (Column 4), total stellar mass of member galaxies (Column 5), and the overdensity measure, defined as $(N - \bar{N})/\sigma_N$ (Column 6).

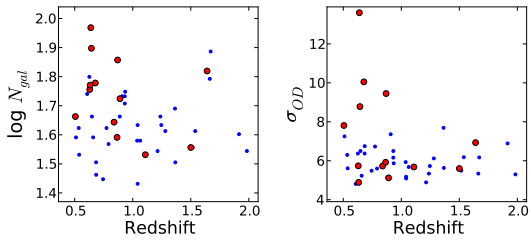

Figure 8. Total number of member galaxies (left panel) and the maximum overdensity factor (right panel) of our galaxy cluster candidates. Red circles are 13 galaxy clusters identified by Finoguenov et al. (2010).

After finding the cluster candidates, we define the spatial center and the redshift of the candidate clusters through the following procedure. At each redshift bin, the mean position, weighted by the galaxy count (N), is found for each connected over-dense structure. Next, the center and the redshift of each cluster candidate is assigned in a similar manner, i.e, as the N-weighted mean center and redshift, for each of the connected redshift bins. Then, we find the galaxies within the radius, $r \leq 1$ Mpc — which corresponds to, or is slightly smaller than, a typical radius of a galaxy cluster — from the center and within the redshift interval, $|\Delta z| \leq 0.028 \times (1 + z)$ — which is the typical redshift error of our data. Finally, we re-calculate the center and the redshift of each cluster candidate as the stellar-mass weighted mean center and redshift of the member galaxies belonging to the overdense area. These center and redshift are the values listed in Columns (1), (2) and (3) in Table 1. The number of member galaxies varies within the range between ∼30 and ∼90 (the left panel of Figure 8). The right panel of the same figure shows the over-density measure, defined as $(N - \bar{N})/\sigma_N$, and shown as σ_{OD} (y-axis) in the figure. Most clusters have σ_{OD} values between 4 and 8, and 4 clusters at redshift $z < 1$ have higher σ_{OD}.

Out of 46 clusters, 13 clusters are also found by Finoguenov et al. (2010) based on the X-ray observation, and they provide the total mass (M_{200}) measured from the X-ray data, and the corresponding r_{200}. We compare the sum of the stellar masses of the cluster member galaxies and their total (halo) mass for these 13 clusters, and these two mass measures — halo mass (M_{200}) and total stellar mass (ΣM_*) — show a positive correlation as shown in the left pane of Figure 9. In the middle panel of this figure, we show the redshift versus the mass ratio ($\Sigma M_*/M_{200}$) of clusters. Here, we cannot see any clear redshift-dependent trend, and the mean mass ratio is 0.013, shown as a blue horizontal line in this panel. The right panel shows the redshift versus M_{200} of our 46 clusters. Here, red large circles are the 13 clusters with their M_{200} taken from Finoguenov et al. (2010). Blue small circles are the remaining 33 clusters, for which we assign a halo mass assuming the stellar-to-halo mass ratio of 0.013. These clusters have halo masses of 3×10^{13} to $2 \times 10^{14}\,\mathrm{M}_\odot$, and total stellar masses of 4×10^{11} to $2 \times 10^{12}\,\mathrm{M}_\odot$.

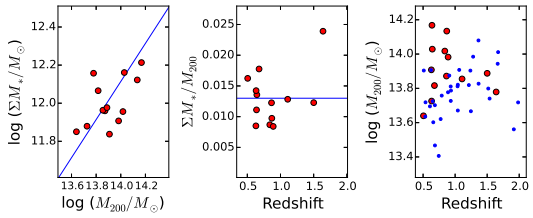

Figure 9. Left: Correlation between the cluster halo mass (M_{200}) and the total stellar mass (ΣM_*) of 13 galaxy clusters which are also identified by Finoguenov et al. (2010). Cluster halo masses are from Finoguenov et al. (2010). As can bee seen here, there exists positive correlation between the total stellar mass and the halo mass. Blue line shows the constant $\Sigma M_*/M_{200}$ ratio of 0.013. **Middle:** The stellar-to-halo mass ratios and their redshifts for the same 13 galaxy clusters. **Right:** Cluster halo masses and their redshifts for all 46 galaxy clusters. Red circles are the same 13 galaxy clusters shown in left two panels. Blue small circles are the remaining 33 clusters. For these 33 clusters, we assume the stellar-to-halo mass ratio of 0.013.

5. COLOR AND STAR FORMATION PROPERTIES

In this section, we take a close look at the color and SF properties of galaxies belonging to the cluster candidates, compare these properties with those of field galaxies in the same UDS field, and investigate their evolutionary trend.

5.1. *Optical Color and its Evolution*

5.1.1. *Color of Cluster and Field Galaxies*

Figure 10 shows $(u - g)_0$ color versus stellar mass diagrams of member galaxies of each cluster candidate. As shown in this figure, the red sequence is formed throughout the whole redshift range, while the fraction of the

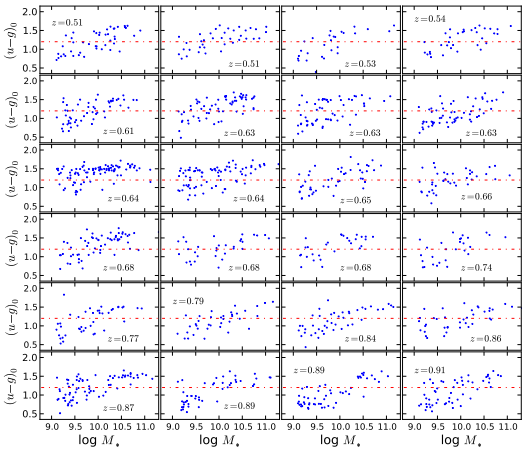

Figure 10. The $(u-g)_0$ versus M_* plots of cluster member galaxies. Each panel shows the color-mass diagram for each individual cluster candidates. In each panel, the redshift of the cluster is given. Red dot-dashed line in each panel shows the dividing line ($(u-g)_0 = 1.2$) between the red and the blue galaxies.

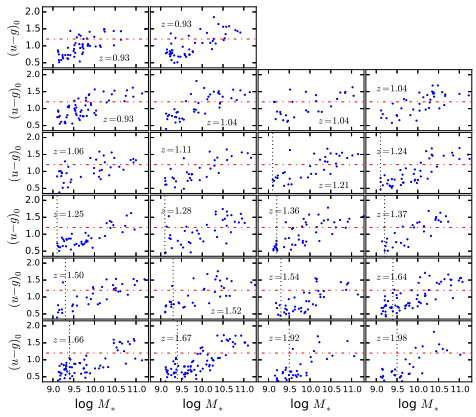

Figure 10. Continued. Black vertical dotted line in each panel shows the stellar mass limit (shown as red curves in Figure 5) at corresponding redshift. We do not show this limit when it is smaller than 9.1.

galaxies with red color decreases with increasing redshift. Hereafter, we refer the galaxies with $(u-g)_0 > 1.2$ as red galaxies, and the ones with $(u-g)_0 < 1.2$ as blue galaxies. In clusters, a significant *sequence* of red galaxies starts to appear at redshift as high as $z \sim 1.6$.

At the very highest redshift ($z > 1.9$), only several massive galaxies have red (> 1.2) colors while progressively lower mass galaxies join the red sequence with decreasing redshift. At $z \lesssim 1$, we can see that the red sequence is well extended down to very low stellar mass ($\log(M_*/M_\odot) \lesssim 9.5$) in most of the clusters. This is a *cluster* version of downsizing phenomenon, which is also shown in the study of two galaxy clusters (at $z \sim 0.8$ and ~ 1.2) by Nantais et al. (2013). We confirm this trend of mass-dependent timing of red sequence formation with a significantly larger sample. A similar, luminosity-dependent trend in a deficit of red galaxies was suggested earlier by Gilbank et al. (2008). Please note that we can detect red galaxies down to a low-mass limit ($= 10^{9.1} M_\odot$) throughout the redshift range ($0.5 < z < 2.0$), thanks to the very deep optical data from SXDS. Therefore, the dearth of low-mass red galaxies at highest redshift bins is real — i.e., not affected by the magnitude limit of the data.

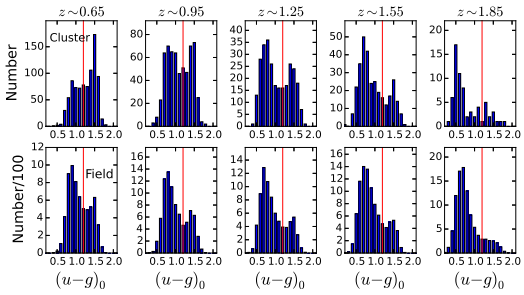

Figure 11. Top: The $(u-g)_0$ color distributions of cluster galaxies in five redshift bins. The cluster galaxies are summed in each redshift bin. **Bottom:** The $(u-g)_0$-distributions of the field galaxies in the same redshift bins as in the top row. The rest-frame color is derived from the best-fit BC03 template for each galaxy. Red vertical line in each panel shows the dividing line ($(u-g)_0 = 1.2$) between red and blue galaxies. Both in cluster- and field-environment, color distributions show clear bimodality, except at the highest redshift bin ($z \sim 1.85$). There is no clear difference in color distribution between clusters and field at the highest redshift while the distributions are clearly distinguished at the lowest redshift ($z \sim 0.65$). The evolution of color distribution in clusters starts to deviate from the field ones from $z \sim 1.25$.

In Figure 11, we present the distributions of $(u-g)_0$ color at five redshift bins ($0.5 \le z < 0.8$, $0.8 \le z < 1.1$, $1.1 \le z < 1.4$, $1.4 \le z < 1.7$, and $1.7 \le z < 2.0$) for cluster (top row) and field galaxies (bottom row). As can be seen in the color-M_* diagrams, $(u-g)_0$ color shows a clear bimodal distribution, which suggests that the color transition of galaxies occurs in a short time scale. At redshifts greater than $z \sim 1.4$, the clusters are dominated by blue galaxies, while at $z \le 0.8$, clusters are *red-dominated* — i.e., majority of the cluster galaxies are red at $z \le 0.8$. But, red galaxies exist even at the highest redshift bin ($z \sim 1.85$). We can also observe the reddening of the peak color of blue galaxies with decreasing redshift, which reflects the evolution of the average stellar population of blue galaxies with time.

When we compare the $(u-g)_0$ color distributions of the cluster galaxies (top row) and of the field galaxies (bottom row), we can see that the color distribution is similar in clusters and in field at the highest redshift bin ($z \ge 1.7$). At $z \le 1.4$, the color distribution in clusters becomes distinguished from that of the field galaxies. Clusters become to be more *red-dominated* compared to field at the same redshift. At the lowest redshift bin, blue galaxies are still the major population in field, while red galaxies clearly dominate in clusters. From this, we can conclude that the color transition of galaxies are accelerated in clusters at redshift lower than $z \sim 1.4$.

5.1.2. *Color Evolution in Clusters and Field*

In Figure 12, we show the redshift evolution of the median color of blue galaxies, both for clusters and field. In this figure, the small green circles show the median color of blue galaxies and the redshift for each cluster candidate, and the red, large circles show the median colors and the median redshifts of blue cluster galaxies summed in each redshift bin. The blue diamonds represent the median values of field blue galaxies at each redshift bin. The corresponding SDSS value, which is

derived from the MPA-JHU catalog[8], is shown as the magenta circle. The expected color evolution of galaxies from the BC03 model with various (delayed) SFHs are also shown as the green dotted lines ($\tau = 1.5$ Gyr, $z_f = 5$), blue dashed lines ($\tau = 2.0$ Gyr, $z_f = 5$), and red solid lines ($\tau = 3.0$ Gyr, $z_f = 8$). Here, z_f is the formation redshift. For each color, the lines from the bottom to the top are with the increasing amount of dust attenuation from $E(B-V) = 0$ with the increment with 0.1.

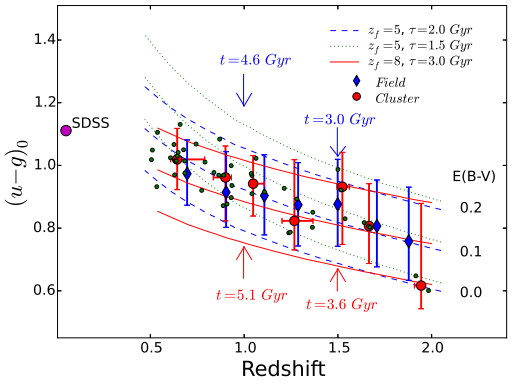

Figure 12. The evolution of the median $(u-g)_0$ color of blue galaxies as a function of the redshift. The small green circles show the median colors of the blue galaxies for each cluster candidate. The large red circles and the blue diamonds are the median $(u-g)_0$ values of blue galaxies in cluster (red circle) and in field (blue diamond). Vertical error bars show the first and the third quartiles, and red horizontal error bars show the range of redshift of individual clusters included at each redshift bin. The magenta circle shows the SDSS value. The lines show the predicted evolution of $(u-g)_0$ colors from BC03 with varying values of τ and $E(B-V)$. The green dotted lines represent the color evolution with $\tau = 1.5$ Gyr and $z_f = 5$, where z_f is the formation redshift. The blue dashed lines are for the color evolution with $\tau = 2.0$ Gyr and $z_f = 5$, and the red solid lines are for $\tau = 3.0$ Gyr and $z_f = 8$. When $z_f = 5$ (blue and green lines), the age (t) is 3.0 Gyr and 4.6 Gyr at $z = 1.5$ and $z = 1$. If $z_f = 8$ (red lines), the ages are 3.6 and 5.1 Gyr at $z = 1.5$ and 1.0. Three lines with same color and style represent the color evolution of templates with $E(B-V) = 0.0$, 0.1, and 0.2 from bottom to top. Solar metallicity is assumed in the case of the synthetic color evolution. This reddening of blue galaxy color with decreasing redshift indicates the average ageing of stellar populations in blue galaxies.

As already mentioned, the blue peak evolves to become redder with decreasing redshift, reflecting the average aging of the stellar population in the blue galaxies. Apparently, the BC03 models with $\tau = 3.0$ Gyr, $z_f = 8$ (with $E(B-V) = 0.0$ and 0.1 — i.e., upper two red solid lines) or the models with $\tau = 2.0$ Gyr, $z_f = 5$ (blue dashed curves) seem to well bracket the observational trend of blue galaxies. This does not necessarily mean that the individual galaxies would evolve with this SFH, even though it can be a representation of global SFH within this redshift range. Interestingly, these SFHs have a peak of SFR at $z \sim 1.8$ or 2, showing a coincidence with the peak of the global SFR density evolution. It should be noted that the difference between cluster- and field-galaxies is not significant, considering the associated ranges of error bars and the fact that median $(u-g)_0$ color can be affected by non-negligible fraction of green galaxies.

In interpreting this color evolution of blue galaxies, we should consider the fact that the blue galaxy population is not a closed one. As galaxies evolve to become redder, these galaxies would move out to the red galaxy population. Also, low mass blue galaxies that were originally out of our mass-cut would be progressively included into the blue galaxy population as their stellar mass grows. The effect of these is to prevent the median color of the blue galaxy population from being reddened quickly. Therefore, it is very likely that the SFRs of the blue galaxies would evolve more rapidly (i.e., having smaller value of τ) than the one represented by the red curves in Figure 12. Also, we cannot rule out the possibility of the change in the median dust attenuation values of the blue galaxies with redshift. The distributions of $E(B-V)$ show little, if any, evolution within the redshift range, $0.5 \lesssim z \lesssim 2.0$, with a hint of slight decrease of the mean $E(B-V)$ at the highest redshift bins ($z > 1.6$). If we accept this small amount of evolution of dust attenuation, it means that the higher dust attenuation at lower redshift contributes, to some extent, to the redder color (of the blue galaxies) at lower redshift, requiring larger value of τ. This will compensate, to some extent, the effects of migration of fading galaxies out of the blue population, making our estimation of the (global representative) SFH more robust.

The evolution of the $(u-g)_0$ color of quiescent galaxies is shown in Figure 13. Unlike blue galaxies, the quiescent galaxy population show little color evolution within the redshift range of $0.5 < z < 2.0$ either in clusters or in field. This no-evolution of $(u-g)_0$ color reflects the fact that *new* quiescent galaxies (with the colors bluer than the *existing* quiescent ones) keep joining the quiescent population while the color of the *existing* quiescent galaxies becomes redder with time. The dashed curves with various colors in Figure 13 are the evolutionary path of BC03 quiescent galaxies with various formation redshift. These curves are shown to guide how the $(u-g)_0$ colors would evolve if no additional quiescent galaxies with bluer color join the existing quiescent population. Purple circles are the corresponding SDSS colors in various stellar mass bins — $\log(M_*/M_\odot) = 9.7$ for the bottom one to $\log(M_*/M_\odot) = 11.1$ for the top one with an increment of 0.2 in logarithmic scale. Analysing red galaxy spectra at $z \sim 0.9$ from the Deep Extragalactic Evolutionary Probe 2 (DEEP2), Schiavon et al. (2006) found relatively young ages ($\sim$ 1 Gyr) for these red galaxies with little or no emission lines. One of their interpretation is that blue SF galaxies keep joining this red population continuously (see also Harker et al. 2006; Faber et al. 2007) maintaining their mean stellar population ages young.

5.1.3. *Red Star-forming Galaxies*

The $(u-g)_0$ color and sSFR of galaxies show a broad correlation in a sense that redder galaxies have in general lower sSFR. However, there are a non-negligible fraction of galaxies whose $(u-g)_0$ color is red (> 1.2) but are still forming stars actively. As shown in Figure 14, these red star-forming (SF) galaxies are, on average, dustier, older, and have lower sSFR than blue SF galaxies. No red SF galaxy has sSFR $\gtrsim 10^{-8}$ yr^{-1} to be classified as

[8] http://www.mpa-garching.mpg.de/SDSS/

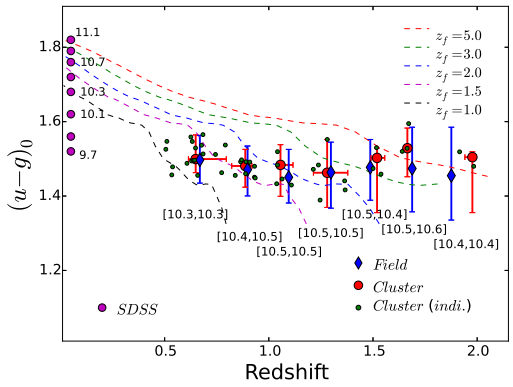

Figure 13. The evolution of the median $(u-g)_0$ color of quiescent galaxies as a function of redshift. The symbol assignment is same as Figure 12. $(u-g)_0$ color of quiescent galaxies shows little evolution within the redshift range, $0.5 < z < 2.0$. This implies that newly quenched galaxies keep joining the quiescent galaxy population within this redshift range. Dashed curves are the evolutionary tracks of quiescent galaxy templates from BC03 with various formation redshift (z_f) as indicated in the figure. Purple circles are the corresponding colors of SDSS galaxies with different stellar masses, which increase from bottom ($\log(M_*/M_\odot) \sim 9.7$) to top ($\log(M_*/M_\odot) \sim 11.1$) with a decrement of 0.2. Bracketed numbers are the median stellar masses at corresponding redshifts for field and cluster galaxies, respectively.

'starbursts'. These indicate that red SF galaxies are in the *fading* stage, and migrating into the red quiescent population.

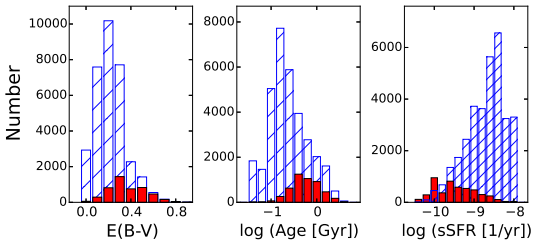

Figure 14. Distributions of dust extinction (E(B-V); **Left**), mean stellar population age (**Middle**), and sSFR (**Right**) estimated from SED-fitting for blue SF (blue hatched histogram) and red SF (red filled histogram) galaxies. On average, red SF galaxies are more dustier as well as older with lower sSFRs.

We investigate the morphological properties of red SF galaxies and compare them with the other galaxy populations to see how many red SF galaxies could be starburst galaxies resulting from gas-rich (wet) merger. A portion of the UDS region ($\sim 22.3' \times 9'$) is covered by the CANDELS (Cosmic Assembly Near-infrared Deep Extragalactic Legacy Survey; Grogin et al. 2011; Koekemoer et al. 2011) program, and observed with the WFC3 (Wide Field Camera 3) on board the *HST*. From the deep WFC3 H-band (F160W) image, which reaches to the 5-σ magnitude limit of 27.45 with FWHM of $0.2''$ (Galametz et al. 2013), the Gini coefficients, G, as well as the M_{20} parameters of the galaxies are measured. Figure 15 shows the distributions of the Gini coefficients and the M_{20} values of the blue, the red SF, and the red quiescent galaxies. The dividing lines between the early-, late-type and major mergers are from Lotz et al. (2008). There are only a few merger candidates among red SF galaxies (in the middle panels, represented as green symbols) and most of the red SF galaxies lie around the boundary between blue (left panels) and red quiescent galaxies (right panels), supporting the idea that these red SF galaxies are in transition phase from blue galaxies to red quiescent ones.

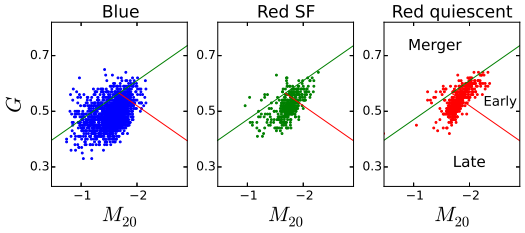

Figure 15. The G-M_{20} diagrams of galaxies in the sub-region of the UDS covered by the CANDELS. **Left column** (blue points): Blue galaxies. **Middle column** (green points): Red SF galaxies. **Right column** (red points): Red quiescent galaxies. The dividing lines are from Lotz et al. (2008). Majority of red SF galaxies lie in the region between blue galaxies and red quiescent ones in this diagram, and only a few red SF galaxies are merger candidates.

We also visually inspect the *HST*/WFC3 images of our galaxies. The blue SF population mostly consists of extended objects with disk-like morphology with small fraction of disturbed ones hinting the recent experience of merger or interaction. On the other hand, red SF galaxies are mixture of disky, spherical, and compact objects, reinforcing that these objects are in transition from blue galaxies into red quiescent ones. In Figure 16, we show example *HST*/WFC3 H-band images of cluster galaxies at $z \sim 0.65$.

5.2. *SF properties and Evolution of Cluster and Field Galaxies*

In previous section, we investigated the rest-frame optical color properties of galaxies in clusters and field. Now, in this section, we concentrate on the SF properties of galaxies and analyse how the SF properties of galaxies within the high-redshift clusters evolve with time and also compare this with that of the field galaxies in the same redshift range.

In Figure 17, we compare the distributions of sSFR of the cluster- and the field galaxies at five redshift bins with the same redshift binning as in the Figure 11. In this figure, we assign sSFR $= 10^{-12}$ yr^{-1} to all quiescent galaxies with sSFR $< 10^{-12}$ yr^{-1}. Similarly with color distribution, the sSFR distribution of SF galaxies in clusters and in the field are similar at high redshift bins ($z \geq 1.4$), while it shows a clear difference from that of the field galaxies at the lowest redshift bin ($z \leq 0.8$). For the quiescent galaxy fraction (over SF ones), the difference between clusters and field starts to show up from $z \sim 1.25$. While the evolutionary trends of sSFR distributions is similar with that of the color distributions shown in Figure 11, the sSFR distribution changes more slowly (especially for the cluster galaxies) than the color distribution. For example, at $z \sim 0.95$, the color distributions are already different between cluster and field, while the sSFR distributions of SF galaxies still remain similar in field- and cluster-environments.

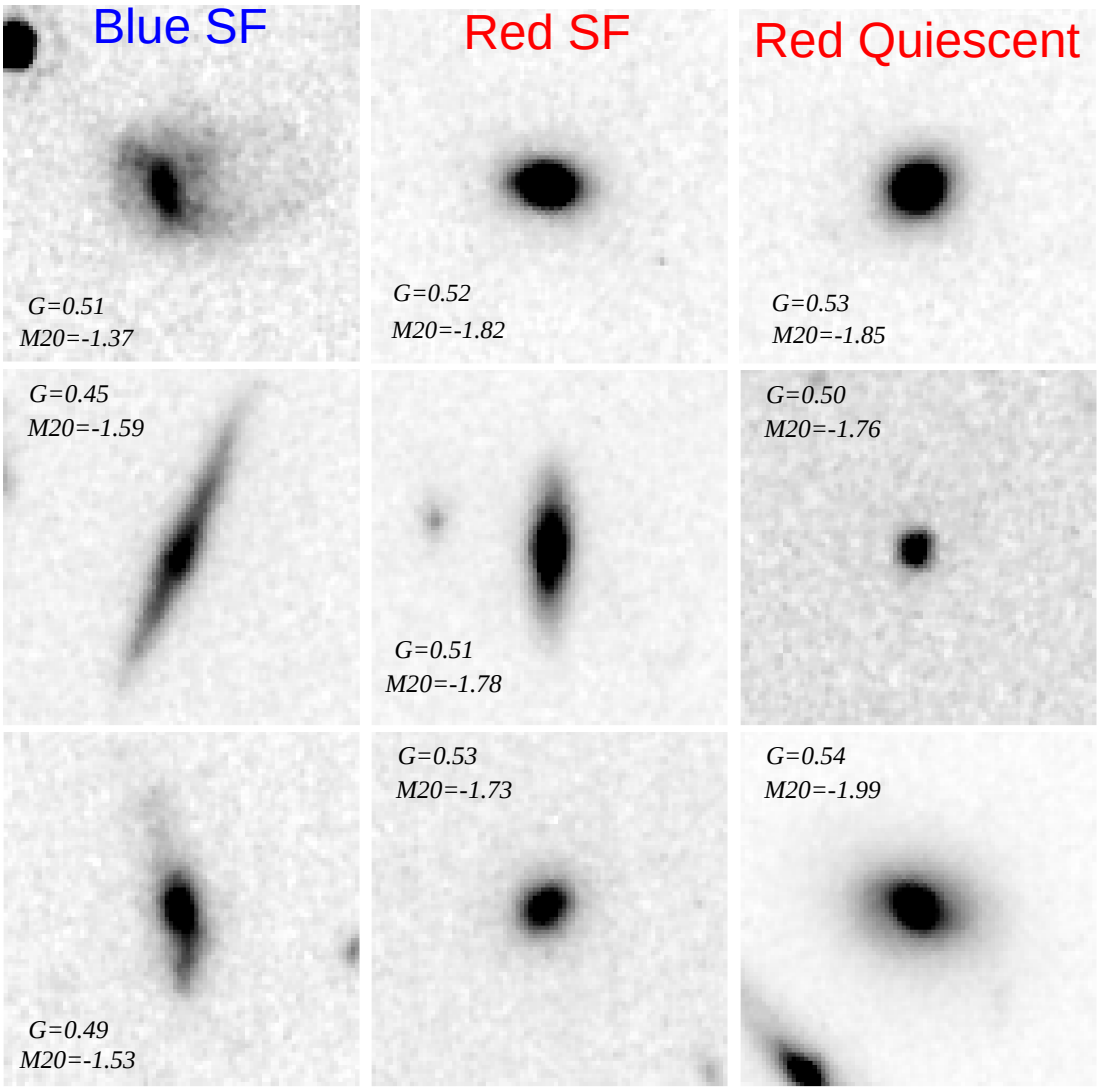

Figure 16. *HST*/WFC3 H-band (F160W) images of cluster galaxies at $z \sim 0.65$. **(Left)** Examples of blue star-forming galaxies. **(Middle)** Red star-forming galaxies. **(Right)** Red quiescent galaxies. Each image cut size is $\sim 5'' \times 5''$. We show the values of Gini coefficient (G) and $M20$ of each galaxy as well.

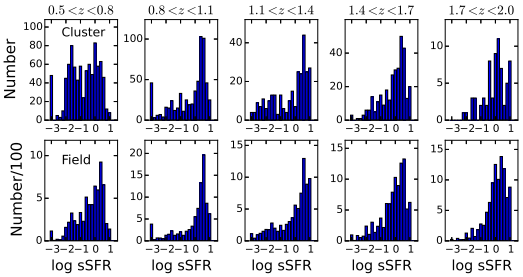

Figure 17. Top: The sSFR distributions of cluster galaxies in five redshift bins. The cluster galaxies are summed in each redshift bin. Bottom: The sSFR distributions of the field galaxies in the same redshift bins as in the top row. The sSFR is given in the unit of Gyr^{-1}. In each panel, we assign $\mathrm{sSFR} = 10^{-3}$ Gyr^{-1} to all quiescent galaxies with $\mathrm{sSFR} \; ¡ \; 10^{-3}$ Gyr^{-1}. The sSFR distribution of cluster SF galaxies shows clear difference from that of field SF galaxies only at the lowest redshift bin ($z \sim 0.65$), while relative fraction of quiescent galaxies shows difference between clusters and field at $z \lesssim 1.4$.

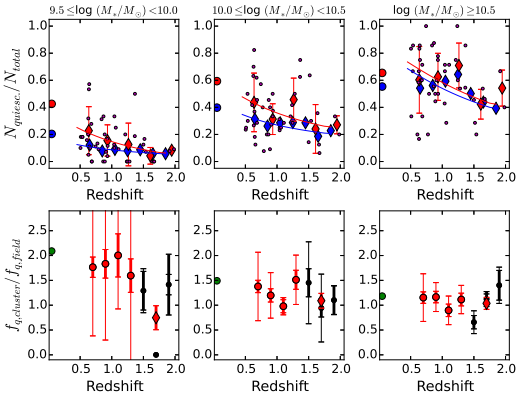

Figure 18. **Upper**: The quiescent fraction evolution of galaxies in three stellar-mass bins (log $M_*/M_\odot \sim 9.75$ (left), 10.25 (middle), and ≥ 10.5 (right). The purple dots show the quiescent galaxy fraction of the individual cluster candidate and the red diamonds with the error bar are the number-weighted mean and the standard deviation of cluster galaxies summed at discrete redshift bins ($\Delta z = 0.3$). The blue diamonds are the quiescent fraction of the field galaxies at each redshift bin ($\Delta z = 0.2$). The red and blue circles in each panel show the cluster and field quiescent fraction at each corresponding stellar mass of the SDSS galaxies from Baldry et al. (2006). The difference of quiescent fraction in different stellar mass bins is greater than the difference between different environment in the same stellar mass bin. Solid curves in each panel show the best-fit quiescent fraction evolution (Equation 4) for cluster (red) and field (blue) galaxies, respectively. **Lower**: The excess of the quiescent fraction in the clusters over the field value, defined as $f_{q,cluser}/f_{q,field}$, where $f_{q,cluster}$ and $f_{q,field}$ are quiescent fraction in the clusters and in the field, respectively. The thick error bars show the standard deviation at each redshift bin, while the thin error bars reflect the spread among clusters in the given redshift bin. We observe this excess becomes significant (> 1.5) only in the smallest mass bin (lower left panel) at $z < 1.2$.

Next, we compare the evolution of the quiescent galaxy fraction in cluster and in field in Figure 18, dividing the sample into three stellar-mass bins : $9.5 \leq \log M_*/M_\odot < 10.0$ (left panel), $10.0 \leq \log M_*/M_\odot < 10.5$ (middle), and $\log M_*/M_\odot \geq 10.5$ (right). In this figure, the filled blue diamonds represent the quiescent fraction of field galaxies at each redshift bin, while the quiescent fraction of individual clusters is shown as magenta dots. At several redshift bins, we sum the cluster galaxies in each z-bin, and calculate the mean and the standard deviation. This is shown as the red diamonds with error bar in the figure. The red and blue circles are for the SDSS (Sloan Digital Sky Survey) galaxies from Baldry et al. (2006). We derive these values from their Equation (9), and choose the values with $\sigma = -0.3$ as field values and $\sigma = 0.9$ as cluster values in that equation. And, we apply the correction for red SF galaxies based on Haines et al. (2008).

From Figure 18, we find several interesting aspects in the evolution of quiescent galaxy fraction. First, the increase of the quiescent fraction slows down from the redshift $z \sim 1.3-1.4$ for galaxies with their stellar mass, log $(M_*/M_\odot) \geq 10$, more significantly for the field galaxies, while it evolves fast from $z \sim 2$ down to $z \sim 1.3$ for massive galaxies ($M_* \geq 10^{10.5} M_\odot$). At the two high stellar-mass bins, the quiescent fraction remains nearly unchanged from $z \sim 1.3-1.4$ both in field and in cluster. Comparison with the local values (the red and the blue circles) shows that the quiescent fraction has already reached to the local value for the most massive galaxies (log $(M_*/M_\odot) \geq 10.5$) at $z \sim 0.6$ both in clusters and in field (the right panel), while the growth of quiescent fraction must be accelerated at $z \lesssim 0.5$ to match the SDSS values in the case of low mass galaxies with log $(M_*/M_\odot) < 10$. This near-constant quiescent fraction of massive galaxies is in good agreement with the previous studies (e.g., Im et al. 2002; Ilbert et al. 2013). This change in the increase of quiescent fraction indicates that the redshift range $z \gtrsim 1.3$ defines the era of the rapid build-up of massive quiescent galaxies, which is in broad agreement with the finding of actively star-forming galaxy clusters at $z > 1.3$ by several authors (e.g., Tran et al. 2010; Zeimann et al. 2012; Santos et al. 2014).

Second, the fraction of quiescent galaxies is higher in clusters than in field at $z < 1.4$ for galaxies with $M_* < 10^{10.5} M_\odot$, even though the scatter among the individual cluster candidates is quite large. From this, we can speculate that the environmental quenching becomes to work more strongly at redshift, $z \lesssim 1.4$, but with a certain amount of cluster-to-cluster variation. Also, we can see that the difference in the quiescent galaxy fraction between the cluster and the field environments is more significant for low-mass (log $(M_*/M_\odot) < 10$) galaxies (the left panel) at redshift $z \lesssim 1$.

Last, as can be seen clearly in this figure, the quiescent fraction is a strong function of the stellar mass rather than their environment. At the highest mass bin, the *cross-over*, which we define as the redshift or the epoch when the quiescent fraction starts to exceed 50 %, occurs already at $z \sim 1.5$. In sharp contrast, in the lowest mass bin, the quiescent fraction never reaches the *cross-over* down to $z \sim 0.5$ both in field and in cluster. Actually, the quiescent fraction is $\lesssim 0.2$ throughout the redshift range in field. This strong mass-dependence of quiescent fraction evolution well agrees with the recent results of Moustakas et al. (2013) — who found a nearly constant number density of massive quiescent galaxies at $z \lesssim 1$ while the corresponding value rises rapidly with decreasing redshift for less massive galaxies, and of Huang et al. (2013). This strong mass dependence and the weaker environmental dependence dictates that the stellar mass plays a more dominant role in shaping the SFH of galaxies than the cluster-specific processes.

To gain an insight how rapidly (or how slowly) star formation is quenched for galaxies with different stellar masses, we devise a simple model explaining the evolution of star-forming galaxy fraction, $f_{sf}(t)$, as follows.

$$f_{sf}(t) = f_{sf}(0) \times (\tfrac{1}{2})^{t/\gamma}, \quad (3)$$

where, $f_{sf}(0)$ is the fraction of SF galaxies at an initial time $t = 0$. In this model, γ is a *half-life* of SF galaxy population, which means that the fraction of SF galaxies becomes half of its initial values after the time $t = \gamma$. This simplified model assumes that the total number of galaxies does not change with time — i.e., no galaxy is added to or removed from the sample, and no merger occurs between galaxies.

Then, the quiescent fraction, $f_{quies.}$ would increase as,

$$f_{quies.}(t) = 1 - f_{sf}(0) \times (\tfrac{1}{2})^{t/\gamma}. \quad (4)$$

We fit our data points to this simple model, and we show this $f_{quies.}$ for the best-fit values of γ's as solid curves in each panel in the upper row of Figure 18. In each panel, the red and the blue curves are for cluster and field galaxies, respectively. For cluster galaxies at $0.5 < z < 2.0$ (solid red curves), the best-fit values for γ are 15 ± 2.2, 9.7 ± 3.6 and 4.4 ± 1.9 Gyr for the lowest, middle and highest stellar-mass bins. In the case of field galaxies (solid blue curves), the corresponding values are 46 ± 7.1, 18 ± 3.9, and 5.2 ± 1.4 Gyr, each. This again demonstrates that: (1) massive galaxies become quiescent more rapidly both in clusters and in field (i.e., having smaller value of γ) than less massive galaxies, and (2) star formation is more rapidly quenched in clusters than in field.

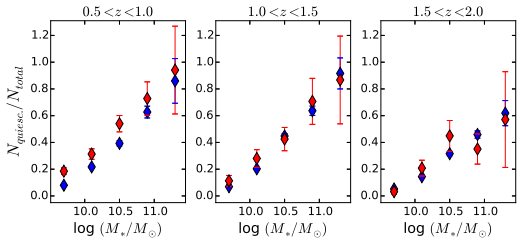

Figure 19. The quiescent fraction evolution of galaxies in three redshift bins ($z \sim 0.75$ (left), 1.25 (middle), and 1.75 (right). The red and blue diamonds with the error bar are the number-weighted mean and the standard deviation of cluster and field galaxies summed at discrete stellar-mass bins, respectively. The clear dependence of quiescent fraction on the stellar-mass can be seen.

The lower panels of Figure 18 show the ratio of the quiescent fraction in clusters ($f_{q,clustesr}$) to that in the field ($f_{q,field}$). Here, we take an average value of the highest three redshift bins (shown as the black circles) and show it as a red diamond in each panel. In the two high mass bins (middle and right panel), the fraction is always $\lesssim 1.5$ with little evolution. However, this fraction increases rapidly with decreasing redshift for low mass galaxies ($\log M_*/M_\odot < 10$), and is higher than that in the higher mass bins at $z < 1.4$. This also indicates that the environmental quenching becomes more significant for low mass galaxies at $z < 1.4$.

To see the effect of stellar mass in determining the quiescent fraction more clearly, we show the stellar-mass dependent quiescent fraction at three redshift bins in Figure 19. In this figure, we can clearly see the strong stellar-mass dependence of the quiescent galaxy fraction at all three redshift bins as well as a clear excess in the quiescent galaxy fraction in clusters compared to the field for low-mass galaxies ($\log (M_*/M_\odot) \lesssim 10.5$) at the lowest redshift bin (left panel).

Summarizing, our investigation of the quiescent galaxy fraction and its evolution reveals several important aspects about quiescent galaxy formation: (1) At $z > 1.3$, quiescent, massive galaxies were built up rapidly, with a similar rate in both clusters and field. By z 1.3, most of the massive,quiescent galaxies were built up. (2) At $z < 1.3$, the environmental dependence of quiescent fraction become visible. The difference between cluster- and field-environment is clearer for low-mass ($\log (M_*/M_\odot) < 10.0$) galaxies. (3) Stellar mass plays more dominant role in determining the quiescent fraction than the environment throughout the entire redshift range.

5.3. *Quenching Efficiency*

In the previous section, we have shown that the quiescent galaxy fraction shows a clear stellar-mass–dependent trend, in a sense that the fraction of quiescent galaxies is higher for more massive galaxies throughout the redshift range, $0.5 \lesssim z \lesssim 2$ (upper panels of Figure 18), and also that the excess of the quiescent galaxy fraction in clusters over field environment is higher for low-mass ($< 10^{10} M_\odot$) galaxies, especially at redshifts lower than $z < 1.2$ (lower panels of Figure 18). Now, we investigate the *environmental quenching efficiency* (e.g. van den Bosch et al. 2008; Peng et al. 2010; Quadri et al. 2012). We define this environmental quenching efficiency as,

$$(f_{q,cluster} - f_{q,field})/f_{sf,field}, \quad (5)$$

where $f_{q,cluster}$ and $f_{q,field}$ are the fraction of quiescent galaxies in clusters and in field, respectively, and $f_{sf,field}$ is the fraction of star-forming galaxies in field ($= 1 - f_{q,field}$). This quantity measures the fraction of SF galaxies in field that would have become quiescent if they were in cluster. Figure 20 shows the evolution of the *environmental quenching efficiency* in different stellar mass bins. Our results shows no clear stellar-mass dependent trend — even though the scatter is larger in the highest mass bin due to the small number of massive galaxies and the small $f_{sf,field}$ values in this mass bin — confirming previous results (Peng et al. 2010; Quadri et al. 2012) but extending the probed redshift range to $z \sim 2$.

How can this result — no significant mass dependence in environmental quenching efficiency — be reconciled with the results in the previous section (e.g., Figure 18) — the high excess of the quiescent fraction in clusters in the lowest mass bin? This difference arises because there is another quenching mechanism — i.e., *mass quenching*. Massive galaxies are affected strongly by mass quenching, and they are mostly quiescent already at $z \sim 1.3$, leaving little room for the environmental quenching to play a significant role. On the other hand, the lower mass galaxies are quenched only mainly through the environment effects that becomes significant at $z < 1.3$.

6. SUMMARY AND CONCLUSION

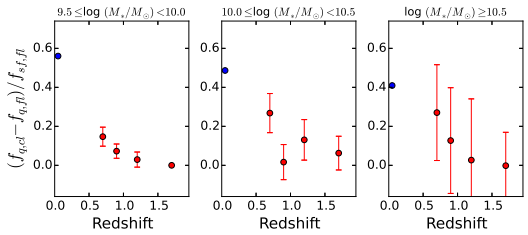

Figure 20. Evolution of environmental quenching efficiency, defined as the excess of quiescent galaxy fraction in clusters over field divided by SF galaxy fraction in field. Three panels show this evolution in different stellar mass bins. Red circles are our results and blue circles are SDSS values. There is no clear difference between different stellar mass bins, except large scatter in the highest mass bin (log $(M_*/M_\odot) \geq 10.5$; right panel).

In this paper, using deep optical to MIR data in the UKIDSS/UDS field, we have found 46 high-redshift galaxy clusters up to $z \lesssim 2$, among which 27 are newly found. We analyse the stellar population properties, such as color and SFR, of galaxies both in cluster and field environments over a wide redshift range to understand the effects of cluster environment on the galaxy evolution.

Through this analysis, we have found that the quiescent galaxy fraction increases rapidly with decreasing redshift at $z \gtrsim 1.3$, and the increase is slowed down at lower redshift for massive (log $(M_*/M\odot) > 10.5$) galaxies. This trend points to the redshift range $z \gtrsim 1.3$ as the era of the rapid build-up of massive quiescent galaxies — the epoch when many massive galaxies stop their star formation and become quiescent. The difference in the quiescent galaxy fraction between clusters and the field increases at $z \lesssim 1.2$-1.4, which coincides with the epoch when the increase in the quiescent galaxy fraction begins to slow down. In this redshift range ($0.5 \lesssim z \lesssim 1.4$), the quiescent galaxy fraction remains nearly unchanged in field, while it keeps increasing in clusters (but more slowly than at $z \geq 1.4$). This difference is only significant for low mass galaxies with log $(M_*/M_\odot) \leq 10.0$.

The environmental quenching efficiency shows no clear stellar-mass dependence, which is in agreement with previous results (e.g., Peng et al. 2010; Quadri et al. 2012), while our results extend this up to higher redshift ($z \sim 2$). However, the effects of environmental quenching appears more significantly for low-mass galaxies, because massive galaxies are affected by another quenching mechanism — i.e., mass-quenching — and most of these massive galaxies are already quenched at $z > 1$.

At $z > 1.4$, the quiescent fraction of galaxies shows no clear dependence on their environment, in contrast to its strong dependence on stellar mass. This infers that the SFH of galaxies is mainly shaped by their stellar mass during the early phase of evolution. The effects of the cluster environment on determining the quiescent fraction of galaxies seem to be more significant for less massive galaxies with $M_* < 10^{10}\,M_\odot$, for which mass quenching does not yet affect their SF activity, at $z < 1.4$. The delayed appearance of the cluster-environment effects on the quiescent galaxy formation for low-mass galaxies implies that the cluster-specific processes which are mainly responsible for the excess of the quiescent fraction in clusters compared to the field region may be gradual, time-taking processes — like the strangulation (Larson et al. 1980; Balogh et al. 2000) — rather than abrupt or violent processes — like ram-pressure stripping, for low-mass galaxies. The investigation of the morphology of red SF galaxies — which shows that the most transition from the blue SF galaxies to red quiescent ones in clusters does not affecting their morphological appearance significantly — supports this idea.

One interesting question is why the SFHs of galaxies are affected by their stellar mass. More specifically, why is the quiescent galaxy fraction higher for more massive galaxies at all environment over a wide range of redshift ($z \lesssim 2$) and without strong environmental dependence? One possible answer is that the dynamical time-scale would be shorter for the galaxies with greater stellar masses than less massive galaxies. If the SFR of galaxies depends on this dynamical time-scale, in a sense that shorter dynamical time-scale leads to higher SFR — as assumed in many galaxy formation models (e.g., Somerville et al. 2012), more massive galaxies will consume their gas more rapidly to arrive the red quiescent galaxy sequence earlier than low mass galaxies. Major mergers between massive SF galaxies can also accelerate this fast gas consumption. Another possibility is that any negative feedback which works preferentially for massive galaxies — such as AGN feedback (e.g. Hopkins et al. 2006; Somerville et al. 2008; Santos et al. 2014) or halo mass quenching (Birnboim & Dekel 2003) — is the driver of the mass-quenching phenomena.

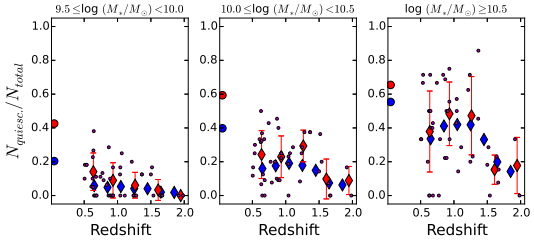

Figure A1. The quiescent fraction evolution of galaxies in three stellar-mass bins (log $M_*/M_\odot \sim 9.75$ (left), 10.25 (middle), and ≥ 10.5 (right) when we apply constant sSFR cut (sSFR $= 10^{-10.7}$ yr^{-1}). The symbol assignment is same as in Figure 18. Similarly with Figure 18, the difference of quiescent fraction in different stellar mass bins is greater than the difference between different environment in the same stellar mass bin in both cases.

One of the interesting results of this work is that the quiescent galaxy fraction drops rapidly as we approach the redshift, $z \sim 2$, independent of the environment in which they reside. This result indicates that the majority of galaxies are actively forming stars at $z \gtrsim 2$. Combined with the fact that the quiescent fraction within clusters and in the field are similar at this epoch, this indicates that studies of clusters or proto-clusters at $z \gtrsim 2$ would be crucial in revealing the very initial properties of the forming galaxy clusters as well as the evolution of galaxies in these massive structures. Also, we can expect that any cluster finding methods using the presence of old and quiescent galaxies within clusters (for example, like red-sequence technique) would miss many clusters or proto-clusters at $z \gtrsim 2$. In our work, both of the identification of the galaxy clusters at $z \gtrsim 1.5$, as well as the reliable estimation of the SFR of galaxies through the SED-fitting are possible thanks to the deep NIR data

from the UKIDSS. This implies that reliable NIR (photometric or spectroscopic) data are essential for the future search and the study of the high-redshift galaxy clusters during this important epoch ($z > 1.5$). Therefore, we can expect a big leap in our understanding of the properties and the evolution of the high-redshift galaxy clusters or proto-clusters as well as of the galaxy evolution with the near-future NIR facilities either in space — like JWST (James Webb Space Telescope) — or on the ground — like GMT (Giant Magellan Telescope) with the GMACS (with the NIR-arm) and later with the NIRMOS.

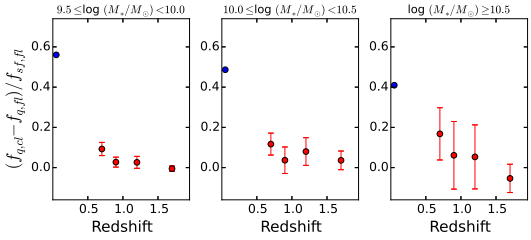

Figure A2. Evolution of environmental quenching efficiency, defined as the excess of quiescent galaxy fraction in clusters over field divided by SF galaxy fraction in field with constant sSFR cut (sSFR $= 10^{-10.7}$ yr^{-1}). The symbol assignment is same as in Figure 20. Three panels show this evolution in different stellar mass bins, and there is no clear difference between different stellar mass bins.

This work was supported by the National Research Foundation of Korea (NRF) grant, No. 2008-0060544, funded by the Korea government (MSIP). The UKIDSS project is defined in Lawrence et al. (2007). The UKIDSS uses the UKIRT Wide Field Camera (WFCAM; Casali et al. 2007). The photometric system is described in Hewett et al. (2006), and the calibration is described in Hodgkin et al. (2009). The pipeline processing and science archive are described in Irwin et al (2009, *in prep*) and Hambly et al. (2008). Part of this work is based on observations taken by the CANDELS Multi-Cycle Treasury Program with the NASA/ESA HST, which is operated by the Association of Universities for Research in Astronomy, Inc., under NASA contract NAS5-26555.

Facilities: UKIRT (WFCAM), Subaru (SUPRIME-CAM), HST (WFC3).

APPENDIX

EFFECTS OF DIFFERENT SSFR CUT

Since galaxies selected with our redshift-dependent cut of $sSFR < 1/3t$ are not quite "quiescent" (i.e., no SF) at high redshift, we examine here how a constant sSFR cut changes our main conclusion regarding SF quenching. Here, we choose a cut of sSFR $= 10^{-10.7}$ yr^{-1}, which corresponds to the cut for local quiescent galaxies (e.g. Gallazzi et al. 2009; Ko et al. 2014).

Applying this constant sSFR cut, we first analyse the evolution of quiescent galaxies fraction. In Figure A1 — which corresponds to upper panels of Figure 18, we show the evolution of quiescent galaxy fraction in different mass bins. Not surprisingly, the quiescent galaxy fraction is overall lower than when we apply the $1/[3t(z)]$-cut. The most significant difference is that the quiescent galaxy fraction shows steeper increase from $z \sim 2$ to $z \sim 1.3$, for galaxies with $M_* \geq 10^{10} M_\odot$ (middle and right panels), especially for $M_* \geq 10^{10.5} M_\odot$, than in Figure 18. This indicates that SF quenching (to local quiescent galaxy level) is faster for more massive galaxies. This fast increase of quiescent fraction at high-z agrees with Domínguez Sánchez et al. (2011) result.

While there are interesting differences in quiescent fraction evolution with different sSFR cuts, one important trend seems to hold: the quiescent galaxy fraction shows clearer dependence on their stellar mass than the environment. The environmental quenching efficiency (Figure A2) is not mass-dependent, but rises toward lower redshift (at $z < 1$), similarly with Figure 20.

REFERENCES

Baldry, I. K. et al. 2006, MNRAS, 373, 469
Balestra, I. et al. 2010, A&A, 512, A12
Balogh, M. L., Navarro, J. F., & Morris, S. L. 2000, ApJ, 540, 113
Balogh, M. L. et al. 2004, MNRAS, 348, 1355
Behroozi, P. S., Wechsler, R. H., & Conroy, C. 2013, ApJ, 770, 57
Bell, E. F., Wolf, C., Meisenheimer, K., Rix, H.-W., Borch, A, Dye, S., Kleinheinrich, M., Wisotzki, L., & McIntosh, D. H. 2004, ApJ, 608, 752
Bertin, E. & Arnouts, S. 1996, A&AS, 117, 393
Birnboim, Y. & Dekel, A. 2003, MNRAS, 345, 349
Blanton, M. R., Eisenstein, D., Hogg, D. W., Schlegel, D. J., & Brinkmann, J. 2005, ApJ, 629, 143
Blanton, M. R. et al. 2003, ApJ, 594, 186
Brammer, G. B., van Dokkum, P. G., & Coppi, P. 2008, ApJ, 686, 1503
Brammer, G. B., van Dokkum, P. G., Franx, M., et al. 2012, ApJS, 200, 13
Bruzual,G & Charlot, S. 2003, MNRAS, 344, 1000 (BC03)
Burgarella, D. et al. 2013, A&A, 554, A70
Butcher, H. & Oemler, A. Jr. 1984, ApJ, 285, 426
Calzetti, D. et al. 2000, ApJ, 533, 682
Casali, M. et al. 2007, A&A, 467, 777
Chabrier, G. 2003, PASP, 115, 763
Cimatti, A. et al. 2008, A&A, 482, 21

Conselice, C. J., Bundy, K., U, V., Eisenhardt, P., Lotz, J., & Newman J., 2008, MNRAS, 383, 1366
Cooper, M. C., et al. 2006, MNRAS, 370, 198
Cooper, M. C., et al. 2008, MNRAS, 383, 1058
Cucciati, O., et al. 2006, A&A, 458, 39
Cucciati, O., et al. 2012, A&A, 539, 31
Daddi, E. et al. 2004, ApJ, 617, 746
Daddi, E. et al. 2007, ApJ, 670, 156
Damen, M. et al. 2009, ApJ, 690, 937
Domínguez Sánchez, H., Pozzi, F., Gruppioni, C. et al. 2011, MNRAS, 417, 900
Dressler, A. 1980, ApJ, 236, 251
Dressler, A. et al. 1997, ApJ, 490, 577
Elbaz, D., et al. 2007, A&A, 468, 33
Faber, S. M. et al. 2007, ApJ, 665, 265
Fassbender, R. et al. 2011, A&A, 527, L10
Finoguenov, A. et al. 2010, MNRAS, 403, 2063
Furusawa, H., et al. 2008, ApJS, 176, 1
Galametz, A. et al. 2013, ApJS, 206, 10
Gallazzi, A. et al. 2009, ApJ, 690, 1883
Gilbank, D. G., Yee, H. K. C., Ellingson, E., Gladders, M. D., Loh, Y.-S., Barrientos, L. F., & Barkhouse, W. A. 2008, ApJ, 673, 742
Gobat, R. et al. 2011, A&A, 526, 133
Grogin, N. et al. 2011, ApJS, 197, 35
Grützbauch, R., Conselice, C. J., Varela, J., Bundy, K., Cooper, M. C., Skibba, R., & Willmer, C. N. A. 2011, MNRAS, 411, 929
Gunn, J. E. & Gott, J. R. III, 1972, ApJ, 176, 1
Haines, C. P., Gargiulo, A. & Merluzzi, P. 2008, MNRAS, 385, 1201
Hambly, N. C. et al. 2008, MNRAS, 384, 637
Hanami, H. et al. 2012, PASJ, 64, 70
Harker, J. J., Schiavon, R. P., Weiner, B. J., & Faber, S. M. 2006, ApJ, 647, L103
Hartley, W. G., Conselice, C. J., Mortlock, A. et al. 2014, arXiv:1406.6058
Hartley, W. G. et al. 2013, MNRAS, 431, 3045
Hewett, P. C., Warren, J. J., Leggett, S. K. & Hodgkins, S. T. 2006, MNRAS, 367, 454
Hilton, M. et al. 2010, ApJ, 718, 133
Hodgkin, S. T., Irwin, M. J., Hewett, P. C. & Warren, J. J. 2009, MNRAS, 394, 675
Holden, B. P. et al. 2007, ApJ, 670, 190
Hopkins, A. M. & Beacom, J. F. 2006, ApJ, 651, 142
Hopkins, P. F., Hernquist, L., Cox, T. J., Di Matteo, T., Robertson, B., & Springel, V. 2006, ApJS, 163, 1
Huang, J.-S. et al. 2013, ApJ, 766, 21
Ilbert, O., Capak, P., Salvato, M. et al. 2009, ApJ, 690, 1236
Ilbert, O. et al. 2013, arXiv:1301.3157
Im, M. et al. 2002, ApJ, 571, 136
Jimenez, R., Panter, B., Heavens, A. F., & Verde, L. 2005, MNRAS, 356, 495
Kang, E. & Im, M. 2009, ApJ, 691, L33
Kang, E. & Im, M. 2015, JKAS, 48, 21
Kauffmann, G., White, S. D. M., & Guiderdoni, B. 1993, MNRAS, 264, 201
Kauffmann, G. et al. 2003, MNRAS, 341, 54
Kauffmann, G., et al. 2004, MNRAS, 353, 713
Ko, J. et al. 2014, ApJ, 791, 134
Kodama, T. & Arimoto, N. 1997, A&A, 320, 41
Koekemoer, A. M. et al. 2011, ApJS, 197, 36
Koo, D. C. et al. 2005, ApJS, 157, 175
Larson, R. B. 1974, MNRAS, 166, 385
Larson, R. B., Tinsley, B. M., & Caldwell, C. N. 1980, ApJ, 237, 692
Lawrence, A. et al. 2007, MNRAS, 379, 1599
Le Fèvre, O. et al. 2004, A&A, 428, 1043
Lee, S.-K., Ferguson, H. C., Somerville, R. S., Giavalisco, M., Wiklind, T., & Dahlen, T. 2014, ApJ, 783, 81
Lee, S.-K., Ferguson, H. C., Somerville, R. S., Wiklind, T., & Giavalisco, M. 2010, ApJ, 725, 1644
Lee, S.-K., Idzi, R., Ferguson, H. C., Somerville, R. S., Wiklind, T., & Giavalisco, M. 2009, ApJS, 184, 100
Lewis, I. et al. 2002, MNRAS, 334, 673
Lilly, S. J. et al. 2007, ApJS, 172, 70
Lotz, J. M. et al. 2008, ApJ, 672,177
Madau, P. 1995, ApJ, 441, 18
Madau, P. & Dickinson, M. 2014, ARA&A, 52, 415
Magnelli, B. et al. 2013, A&A, 553, A132
Maraston, C., Pforr, J., Renzini, A., Daddi, E., Dickinson, M., Cimatti, A., & Tonini, C. MNRAS, 2010, 407, 830
McCracken, H. J., Milvang-Jensen, B., Dunlop, J., et al. 2012, A&A, 544,1 56
Merson, A. I. et al. 2013, MNRAS, 429, 556
Messias, H., Afonso, J., Salvato, M., Mobasher, B., & Hopkins, A. M. 2012, ApJ, 754, 120
Mignoli, M. et al. 2005, A&A, 437, 883
Moore, B., Lake, G., & Katz, N. 1998, ApJ, 495, 139
Moustakas, J. et al. 2013, ApJ, 767, 50
Muzzin, A. et al. 2012, ApJ, 746, 188
Nantais, J. B. et al. A&A, 556, 112
Newman, J. A., Cooper, M. C., Davis, M., et al. 2013, ApJS, 208, 5
Oke, J. B. 1974, ApJS, 27, 21
Pacifici, C., Kassin, S. A., Weiner, B., Charlot, S., & Gardner, J. P. 2013, ApJ, 762, L15
Papovich, C., Finkelstein, S. L., Ferguson, H. C., Lotz, J. M., & Giavalisco, M. 2011, MNRAS, 412, 1123
Papovich, C. et al. 2010, ApJ, 716, 1503
Patel, S. G., Holden, B. P., Kelson, D. D., Illingworth, G. D., & Franx, M. 2009, ApJ, 705, 67

Peng, Y.-J., Lilly, S. J., Kovač, K., et al. 2010, ApJ, 721, 193
Pforr, J., Maraston, C., & Tonini, C. 2012, MNRAS, 422, 3285
Poggianti, B. M. et al. 2001, ApJ, 563, 118
Popesso, P., Dickinson, M., Nonino, M., et al. 2009, A&A, 494, 443
Pozzetti, L. et al. 2003, A&A, 402, 837
Quadri, R. F., Williams, R. J., Franx, M., & Hildebrandt, H. 2012, ApJ, 744, 88
Santos, J. S., Altieri, B., Tanaka, M. et al. 2014, MNRAS, 438, 2565
Schiavon, R. P. et al. 2006, ApJ, 651, L93
Scoville, N. et al. 2013, ApJS, 206, 3
Silverman, J. D. et al. 2010, ApJS, 191, 124
Smail, I., Sharp, R., Swinbank, A. M., Akiyama, M., Ueda, Y., Foucaud, S., Almaini, O. & Croom, S. 2008, MNRAS, 389, 407
Smith, G. P., Treu, T., Ellis, R. S., Moran, S. M., & Dressler, A. 2005, ApJ, 620, 78
Sobral, D., Best, P. N., Smail, I., Geach, J. E., Cirasuolo, M., Garn, T., & Dalton, G. B. 2011, MNRAS, 411, 675
Sobral, D. et al. 2014, MNRAS, 437, 3516
Somerville, R. S. & Primack, J. R. 1999, MNRAS, 310, 1087
Somerville, R. S., Gilmore, R. C., Primack, J. R., & Domínguez, A. 2012, MNRAS, 423, 1992
Somerville, R. S., Hopkins, P. F., Cox, T. J., Robertson, B. E., & Hernquist, L. 2008, MNRAS, 391, 481
Strateva, I. et al. 2001, AJ, 122, 1861
Strazzullo, V. et al. 2013, ApJ, 772, 118
Szokoly, G. P., Bergeron, J., Hasinger, G., et al. 2004, ApJS, 155, 271
Tal, T. et al. 2014, ApJ, 789, 164
Tran, K.-V. et al. 2010, ApJ, 719, L126
Ueda, Y., et al. 2008, ApJS, 179, 124
van Breukelen, C. et al. 2006, MNRAS, 373, L26
van Breukelen, C. et al. 2007, MNRAS, 382, 971
van den Bosch, F. C., Aquino, D., Yang, X. et al. 2008, MNRAS, 387, 79
van der Wel, A. et al. 2007, ApJ, 670, 206
Vanzella, E., Cristiani, S., Dickinson, M., et al. 2008, A&A, 478, 83
Wiklind, T., Dickinson, M., Ferguson, H. C., Giavalisco, M., Mobasher, B., Grogin, N. A., & Panagia, N. 2008 ApJ, 676,781
Wolf, C., Meisenheimer, K., Rix, H.-W., Borch, A., Dye, S., & Kleinheinrich, M. 2003, A&A, 401, 73
Yang, G. et al. 2014, ApJS, 215, 27
York, D. G., Adelman, J., Anderson, J. E., et al. 2000, AJ, 120, 1579
Zeimann, G. R. et al. 2012, ApJ, 756, 115
Zirm, A. W. et al. 2008, ApJ, 680, 224

Table 1
Candidate high-redshift galaxy clusters in the UDS

RA (1)	dec. (2)	z (3)	N_{gal} (4)	ΣM_* (5)	σ_{OD} (6)	Reference (7)
34.48571	-4.88290	0.506	46	7.08	7.81	1
34.66831	-5.05773	0.511	39	10.42	7.25	
34.05109	-4.74287	0.534	42	5.61	6.30	
34.70426	-5.14720	0.538	34	6.80	5.61	
34.54121	-5.36501	0.607	55	6.44	4.81	2
34.54105	-5.26098	0.626	63	10.48	6.37	
34.35041	-5.41133	0.629	57	6.88	5.74	1
34.19640	-5.15057	0.633	59	7.57	4.89	1,2
34.39710	-5.22284	0.639	93	16.34	13.60	1,2
34.60152	-5.41210	0.644	79	14.49	8.78	1
34.51734	-5.52098	0.648	46	6.90	6.50	
34.63576	-4.96694	0.659	39	5.20	5.23	2
34.47932	-5.45278	0.677	60	11.63	10.05	1
34.74237	-5.12341	0.684	32	6.54	6.37	
34.37319	-4.68903	0.685	29	3.81	6.75	
34.84291	-4.82145	0.744	28	3.31	5.49	
34.45845	-5.50699	0.774	42	5.43	6.73	
34.42685	-5.09312	0.791	37	7.44	5.60	
34.52339	-4.73828	0.839	44	9.04	5.73	1
34.82770	-5.08506	0.865	39	9.12	5.92	1
34.63694	-5.01183	0.869	72	13.25	9.45	1
34.16359	-4.73395	0.889	46	7.78	5.12	
34.84166	-4.88236	0.890	53	8.08	5.12	1
34.34870	-5.20672	0.909	54	9.74	7.36	
34.05085	-4.87705	0.931	54	8.41	6.16	
34.06289	-4.71558	0.932	51	6.93	6.50	
34.53990	-5.01259	0.935	56	7.96	5.87	2
34.03834	-5.10964	1.042	43	8.61	5.18	
34.29435	-4.79312	1.042	27	6.09	5.09	2
34.59195	-4.97802	1.038	38	8.43	5.93	
34.52635	-5.01766	1.064	38	10.51	5.68	2
34.28226	-4.82255	1.109	34	9.19	5.68	1
34.61517	-4.69712	1.214	35	8.57	4.89	
34.69049	-4.71229	1.238	46	10.41	5.34	
34.80897	-4.93465	1.246	43	6.03	5.73	
34.53326	-5.01095	1.281	41	12.55	6.12	3
34.85731	-4.86560	1.364	49	15.61	7.69	
34.84134	-4.72292	1.366	32	8.73	5.63	
34.53797	-5.01744	1.500	36	9.48	5.60	1,3
34.07070	-5.00289	1.517	36	8.18	5.49	
34.81516	-4.74594	1.538	41	7.15	6.18	
34.59165	-5.16940	1.640	66	14.37	6.93	1,4
34.17832	-5.15493	1.664	62	11.41	5.34	
34.80031	-4.73156	1.671	77	13.34	6.17	
34.73531	-5.04661	1.916	40	4.73	6.89	
34.72378	-5.17741	1.983	35	6.79	5.30	

Note. —
(1) RA in degree
(2) Declination in degree
(3) Redshift
(4) Number of galaxies within 1 Mpc radius from the cluster center
(5) Sum of the stellar masses of the member galaxies in 1e+11 $M_{\odot}$
(6) Overdensity measure, $(N - \bar{N})/\sigma_N$
(7) Reference list:
1. Finoguenov et al. 2010, *MNRAS*, 403, 2063
2. van Breukelen et al. 2006, *MNRAS*, 373, L26
3. van Breukelen et al. 2007, *MNRAS*, 382, 971
4. Papovich et al. 2010, *ApJ*, 716, 1503